Research Square

Preprints are preliminary reports that have not undergone peer review.
They should not be considered conclusive, used to inform clinical practice,
or referenced by the media as validated information.

Size-Dependent Thermomechanical Vibration Analysis of Porous Functionally Graded Magneto–Electro–Elastic Nanoplates within a Nonlocal Strain-Gradient Framework

Turan Das

turandas@karabuk.edu.tr

Karabuk University

Research Article

Keywords: Nonlocal strain-gradient elasticity, Thermomechanical vibration, Magneto–electro–elastic nanoplates, Functionally graded materials, Porous nanostructures, Size-dependent behavior

Posted Date: April 24th, 2026

DOI: https://doi.org/10.21203/rs.3.rs-9272059/v1

License: This work is licensed under a Creative Commons Attribution 4.0 International License.
Read Full License

Additional Declarations: No competing interests reported.

Size-Dependent Thermomechanical Vibration Analysis of Porous Functionally Graded Magneto–Electro–Elastic Nanoplates within a Nonlocal Strain-Gradient Framework

Turan Das[1,*]

[1] *Department of Mechanical Engineering, Karabuk University, Karabuk, Turkey*

[*]Corresponding author: turandas@karabuk.edu.tr

Abstract

In this study, a size-dependent thermomechanical vibration theory for porous functionally graded magneto-electro-elastic (FG-MEE) nanoplates in the hybrid nonlocal strain gradient theory is proposed. The formulation accounts for temperature rise, electroelastic, and magnetostrictive coupling effects in conjunction with nonlocal and strain gradient effects. The gradations in the material properties in the direction transverse to the plate are described using a power law distribution. The formulation is based on Hamilton's principle. The final governing equation is solved using a harmonic exponential method to obtain an eigenvalue problem. The results are presented in terms of a dimensionless frequency parameter. The influence of porosity index and porosity distribution patterns (FOAM I, FOAM II, and FOAM III) in conjunction with material gradations on the dimensionless frequency parameter is presented in detail. The results show that an increase in porosity index reduces the frequency. The degradation in frequency is found to depend sensitively on the porosity distribution patterns. FOAM I shows the maximum degradation in frequency and approaches complete failure at a lower value of temperature rise. An increase in temperature reduces the frequency. The nonlocal theory shows a stiffness degradation tendency. The stiffness degradation tendency increases with an increase in temperature. The magnetic actuation is found to increase the stiffness and delays degradation. The electric actuation can cause degradation depending upon the dominance of the active phase. The elevated temperature cases are presented to show the stability tendency. In practice, it should be noted that the Curie temperature should be taken into consideration to ensure functionality.

Keywords: Nonlocal strain-gradient elasticity; Thermomechanical vibration; Magneto–electro–elastic nanoplates; Functionally graded materials; Porous nanostructures; Size-dependent behavior.

Introduction

The rapid miniaturization of smart structures has driven the basic incorporation of multifunctional nanoplates in nanoelectromechanical frameworks (NEMS), nanosensors, nanoresonators, nanoactuators and other sleek multi-field gadgets where high affectability and tunable coupled responses are required. Conversely, the irresistible coupling between mechanical, electric and magnetic fields of the magneto–electro–elastic (MEE) nanostructures has drawn great interest because better control and functional adaptability at small scales can be achieved [1,2]. Due to the intense multi-field interactions and the high surface-to-volume ratio at nanoscale, MEE nanoplates exhibit an extreme sensitivity in mechanical response with respect to combined mechanical–thermal–electric–magnetic stimuli. Hence, the establishment of precise theoretical models to illustrate vibration and stability trends under coupled multi-physics scenarios is crucial for reliable design and performance prediction of these smart nanostructures [3–5]. For resonant nanosensing and nanoactuation, the eigenfrequencies and corresponding modes of deformation are important determinants of sensitivity and performance stability, as resonance-based operation is inherently controlled by eigenproperties. Thus, even small offsets in predicted eigenfrequencies are amplified into significant errors in resonance-based estimation and calibration[6,7], particularly with coupled multi-physics effects. This incentive resulted in a plethora of size-dependent investigations on vibration and buckling behavior of nano-beams and nano-plates where the nonlocality, strain-gradient effects, material gradation, porosity and multiple source stimuli have been really focused [5,8–11].

In addition to the above-mentioned performance criteria for the resonance-based responses, actual nano-resonators may experience a coupled condition of thermal drift and electromagnetic actuation, in which any small change in eigenfrequencies may affect the accuracy of the calibration process, modal selectivity, and/or cause cross-talk between modes. For instance, temperature-induced degradations in stiffness, as well as thermally induced in-plane stress, have been demonstrated to cause significant changes in natural frequencies as well as stability boundaries for sophisticated nano-structured materials [5,12]. For magneto-electro-elastic nano-elements, the presence of applied electric and magnetic fields induces additional field-dependent stiffness that can be exploited for frequency tunability while increasing the sensitivity to coupled perturbations from electro-magnetic fields [13]. The above drift effects may be more pronounced for porous materials as well as for functionally graded materials, in which the redistribution of stiffness as well as the amplification of local compliance may cause frequency susceptibility for coupled loading conditions [11,13]. In addition, size-dependent

formulations that account for nonlocal as well as strain gradient effects may cause modified stability boundaries as well as increased sensitivity of higher modes for nanoplates. Therefore, thermo-electro-magnetic robustness should be considered as a critical design criterion similar to frequency tunability for porous FG magneto-electro-elastic nanoplates under coupled thermo-electro-magnetic loading conditions [14,15].

Despite these modeling efforts, classical, scale-free continuum elasticity fails to capture experimentally observed and atomistically predicted size effects in nano-scale structures. To overcome this limitation, nonlocal elasticity introduces long-range interactions through spatially dependent constitutive relations, typically leading to stiffness softening, whereas strain-gradient theories incorporate intrinsic material length scales via higher-order strain terms and are often associated with stiffness hardening [3,16]. However, when employed separately, each formulation may only partially represent the observed size-dependent response. This limitation has motivated the development of hybrid nonlocal strain-gradient theories (NSGT), in which two independent length-scale parameters account simultaneously for long-range nonlocal interactions and microstructural strain-gradient mechanisms within a unified continuum framework [3,8]. Such higher-order NSGT formulations have been successfully applied to size-dependent vibration and stability analyses of beams and plates, including porous and functionally graded configurations under thermal and hygro-thermal environments [8,17]. For porous FG nanoplates in particular, NSGT has demonstrated improved physical consistency in predicting the competing softening–hardening behavior arising from nonlocal and strain-gradient effects, respectively [1,8]. The emerging evidence of analytical and numerical studies conducted under the NSGT paradigm shows that the nonlocal parameter generally controls the attenuation of stiffness, whereas the strain gradient parameter provides an intrinsic stabilizing effect, leading to a typical stiffness-softening versus stiffness-hardening competition in the nano-scale structural response [18–22]. The regular appearance of this dual-length-scale behavior in the independent beam and plate theories supports the physically viable potential of the hybrid approach in modeling nano-scale structures.

Despite these advances having greatly improved the potential of the size-dependent theory of continuum mechanics, its extension to magneto-electro-elastic nanoplates would introduce additional complexity due to the coupled electromechanical and magnetomechanical interactions in these materials [5,23]. In these materials, the intrinsic length scale effects would not occur in isolation but would interact with the temperature-dependent material degradation,

thermal membrane stresses, and stiffness contributions due to electromechanical and magnetomechanical actuations [24,25]. Past studies conducted under the NSGT paradigm have consistently shown that the nonlocal parameter would generally introduce a stiffness-softening tendency in the nanostructures, whereas the strain gradient parameter would introduce an intrinsic hardening effect [9,22]. However, when these competing scale effects are coupled with thermo-electromechanical interactions, the effective rigidity contours and stability bounds of MEE nanostructures may change in a non-trivial manner [5,26]. Hence, a unified theory that can effectively incorporate the scale parameter interactions with coupled thermo-electromechanical effects would be vital for physically viable thermo-vibrational assessment of these nanostructures [27,28].

For instance, within the specific area of multilayer elastic energy systems and smart nanoplates, a number of recent research studies have been conducted to incorporate nonlocal strain gradient theories (NSGTs) and nonlocal strain gradient-based shear deformation theories. Thai et al. developed isogeometric nonlocal strain gradient-based models for the free vibration analysis of functionally graded multilayer elastic energy (MEE) systems and carbon nanotube-reinforced MEE nanoplates, respectively, to demonstrate the competing effects of nonlocal softening and strain gradient hardening parameters on the natural frequencies of these smart systems [22,29]. Roodgar Saffari et al. extended nonlocal strain gradient theories to analyze the free vibration characteristics of sandwich functionally graded porous variable thickness MEE nanoplates, demonstrating that scale parameters, porosity, and gradation parameters significantly influence the free vibration characteristics of smart systems. Nonlocal strain gradient-based thermomechanical vibration models for functionally graded MEE nanoplates under coupled field conditions have also been developed [30]. However, a considerable number of nonlocal strain gradient-based research studies on functionally graded MEE plates are limited to isothermal and mechanically coupled fields, and nonlocal strain gradient-based models are yet to incorporate thermal, porosity, and functional gradation characteristics simultaneously [7]. It is worth mentioning that, for functionally graded smart systems, thermal fields and electro-magnetic fields are coupled phenomena rather than independent phenomena, and temperature-dependent stiffness degradation and thermally induced in-plane stresses significantly change the effective stiffness landscape, natural frequencies, and stability characteristics [31,32]. Concurrently, electro-magnetic potential fields also introduce new stiffness components and coupled fields, which may either enhance or suppress thermal effects based on the specific active phase. These coupled phenomena are more significant for functionally graded systems,

wherein porosity and gradation characteristics amplify stiffness degradation and compliance characteristics [27,33,34]. In addition, size effects in nonlocal and strain gradient elasticity theory suggest that there is an enhanced sensitivity in higher modes and stability characteristics at the nanoscale [33,35,36]. The above results demonstrate that it is not possible to deal with thermo-electro-magnetic interactions sequentially; rather, it is important to develop coupled formulations that can incorporate all these effects in a unified manner. [31,32,35,36].

Thermomechanical coupling has a major influence on the vibration behavior of the structure at the nanoscale, especially for structures exposed to harsh or fluctuating thermal conditions [37,38]. This influence is more prominent for nano-resonant structures exposed to thermal gradients, start-stop thermal excitation, or localized joule heating, wherein thermo-induced in-plane membrane forces play an important role in modifying the stiffness map of the system and assessing proximity to instability [39–41]. An increase in temperature reduces the effective stiffness of the system due to changes in the thermo-mechanical properties of the system, induces in-plane stresses due to thermal loading, and may also cause the system to approach thermal buckling; therefore, thermo-vibrational modeling of the system is of utmost importance [2,5,42]. For functionally graded sandwich nanoplates, Daikh et al. found that the nonlocal parameter as well as the temperature difference reduces the dimensionless natural frequencies of the system effectively [42]. In a similar problem of hygrothermal loading, Fenjan et al. found that an increase in temperature as well as moisture content along with porosity and size-dependent parameters reduces the normalized frequencies significantly, making the system more prone to thermal buckling instability [8].

For instance, in microelectromechanical systems, thermomechanical vibration and buckling behaviors are significantly influenced by temperature-dependent material properties and magneto–electro–elastic coupling effects. The natural frequencies and critical buckling temperatures of various nanostructures, including nano-beams, plates, and sandwich nanoplates, show significant dependence on temperature-dependent properties, including elastic, piezoelectric, and piezomagnetic coefficients. Temperature increase generally results in a decrease in baseline stiffness, nondimensional frequencies, and critical buckling loads, as well as an increase in the relative importance of field-induced forces on system dynamic behavior [23,43]. The presence of porosity and functionally graded configurations also introduces a grading index, porosity level, and auxetic and foam cores, which may affect thermal softening and instability behaviors. However, magneto–electro–elastic coupling effects introduce

directional stiffness properties, which are generally stabilizing when magnetic potential is increased in magnetically dominant phases, and destabilizing when electric potential is increased in electro-elastic-dominated phases [2,23,26,35]. Esen and Özmen formulated an NSGT-based thermomechanical vibration and buckling model for porous FG-MEE nanoplates and demonstrated that increasing temperature and porosity reduce natural frequencies and critical loads, while nonlocal parameters promote stiffness softening and strain-gradient effects provide partial hardening compensation [5]. Aktas et al. incorporated temperature-dependent properties in smart sandwich nanoplates with auxetic cores and MEE face layers, highlighting the sensitivity of thermomechanical responses to both size-dependent parameters and auxetic geometric effects [2]. Comparable influences of porosity distribution, external field potentials, and NSGT scale parameters have also been reported for porous MEE sandwich nanoplates and magnetically actuated sandwich nanobeams [10,11,44]. Despite these advances, many existing thermomechanical vibration analyses employ purely nonlocal or classical theories [4] or focus on non-porous or macroscopically homogeneous MEE layers. Comprehensive size-dependent thermomechanical models for porous FG-MEE nanoplates within a hybrid nonlocal strain-gradient framework therefore remain limited.

Functionally graded materials (FGMs) have been widely adopted in micro- and nano-structural design due to their through-thickness material gradation, which enables tailored stiffness distributions and improved thermo-mechanical performance [42,45–47]. Moreover, foam-based FGM face layers have also been studied for sandwich-type nanoplate models [48]. When combined with porosity, FG material configurations offer further benefits for weight reduction and improved material properties. Porous FG nanoplates have been extensively studied for various types of mechanical, thermal, and hygro-thermal loadings using nonlocal theory and NSGT formulations. It has consistently been shown that increased levels of porosity lead to a reduction in effective stiffness, natural frequencies, and stability [8,49,50]. Despite extensive studies on sandwich-type nanoplate models, porous FG-MEE nanoplates have remained relatively uninvestigated; yet these offer a simple yet versatile framework for investigating various coupled effects of porosity distribution, gradation profile, and intrinsic length scale parameters.

At the nanoplate level, various researchers have also studied nanoplates incorporating porosity within NSGT formulations. Fenjan et al. studied hygro-thermal vibration behavior for porous FG nanoplates using NSGT formulations, revealing strong coupling effects between porosity

and intrinsic scale parameters [8]. Sobhy et al. presented a refined quasi-3D NSGT model for FG porous nanoplates and observed high sensitivity of nanoplate vibration characteristics to porosity levels and scale parameters [49]. Roodgar Saffari et al. studied FG porous variable thickness core sandwich nanoplates using MEE theory and revealed strong coupling effects between porosity distribution and scale parameters on nanoplate free and forced vibration behavior due to electro-magnetic potentials [7]. At the nanobeam level, Pehlivan et al. observed strong effects of various porosity models on the size-dependent thermomechanical vibration behavior for FG MEE nanobeams [11]. Nevertheless, many porous FG nano-models either fail to incorporate full magneto-electro-elastic coupling effects, study a few specific loading conditions, or only study sandwich-type FG nanoplate models.

MEE materials, typically realized as composites of piezoelectric and piezomagnetic phases such as $BaTiO_3$ and $CoFe_2O_4$, exhibit strong coupling among mechanical, electric, and magnetic fields [22]. This intrinsic multi-field interaction enables tunable dynamic behavior through externally applied electric and magnetic potentials, making MEE nanoplates attractive for nanosensors, resonators, and nano-actuators [1,26,51]. Zur et al. developed a nonlocal higher-order shear deformation model for FG-MEE nanoplates and demonstrated that applied electric and magnetic potentials significantly influence vibration and buckling responses [52]. Gholami et al. proposed a size-dependent nonlocal METE nanoplate model and showed that electric and magnetic fields, combined with temperature rise, modify natural frequencies and critical loads [4].

More recently, NSGT-based formulations have been adopted to capture both softening and hardening size effects. Thai et al. applied NSGT within isogeometric and meshfree frameworks to FG-MEE and CNT-reinforced MEE nanoplates, demonstrating that natural frequencies depend on the relative magnitudes of nonlocal and strain-gradient parameters as well as on electric voltage and magnetic potential [22,29]. Esen and Özmen and Pehlivan et al. further incorporated porosity and temperature-dependent properties, highlighting the coupled influence of size parameters, porosity, and magneto–electro–elastic interactions on thermomechanical vibration and buckling behavior [5,11,26]. Comparable sensitivities to applied fields and scale parameters have also been reported for smart sandwich nanoplates with auxetic or foam cores and MEE face layers [2,10,11].

In particular, the thermo-mechanical vibrations and buckling of porous functionally graded magneto-electro-elastic (MEE) nanostructures subjected to electric and magnetic fields have been studied under the NSGT approach in the works of Esen and Özmen [5,26] and Roodgar Saffari et al. [7]. However, these studies are still more or less parametric in nature and are limited to sandwich-type structures, moving load problems, or porosity models used in the studies. A unified thermo-mechanical model for single-layer porous functionally graded magneto-electro-elastic nanostructures considering porosity patterns, functionally graded materials, competing nonlocal and strain gradient approaches, and coupled electric-magnetic fields simultaneously is still lacking in the literature. Moreover, many studies on the application of the NSGT approach have emphasized the importance of using advanced solution schemes such as the isogeometric approach, meshless methods, DQM, FEM, etc., whereas the role of competing nonlocal and strain gradient parameters under thermo-mechanical vibrations induced by electric-magnetic fields still needs to be addressed under a unified framework [7,16,22,29]. Taken together, these observations indicate that an integrative, size-dependent thermo-vibration framework is needed to quantify how porosity patterns and FG profiles interact with coupled electric–magnetic actuation under realistic thermal environments.

Motivated by these gaps, the present work develops a size-dependent thermomechanical vibration model for porous functionally graded magneto–electro–elastic nanoplates based on nonlocal strain-gradient elasticity. The constitutive relations incorporate mechanical, thermal expansion, electroelastic, and magnetostrictive contributions together with nonlocal and strain-gradient effects, while porosity and functional gradation are represented through modified power-law distributions. Governing equations are derived via Hamilton’s principle using higher-order plate kinematics and subsequently solved for thermomechanically loaded, electrically and magnetically actuated nanoplates. The proposed framework enables systematic assessment of the coupled influence of porosity characteristics, gradation indices, intrinsic length-scale parameters, and external multi-field excitations on dimensionless frequency parameters and thermomechanical stability behavior.

Beyond its theoretical contribution, this integrative formulation provides a rigorous basis for predictive evaluation of nano-scale components operating under combined thermal and electromagnetic environments. Porous FG-MEE nanoplates are increasingly relevant in aerospace and spaceborne micro-systems, rocket engine control modules, high-sensitivity gas sensing platforms, and flexible or wearable multi-field technologies, where frequency stability

under thermo–electro–magnetic actuation is critical. In such applications, the interaction among intrinsic length scales, material gradation, porosity distribution, and coupled electric–magnetic fields may directly influence resonance drift, stability margins, and actuation reliability. Therefore, the present unified framework may serve as a consistent theoretical foundation for the design and optimization of next-generation smart nano-structured components subjected to realistic multi-physics operating conditions.

It is worth emphasizing that the elevated thermal conditions considered herein are primarily intended to elucidate thermally induced stiffness degradation, buckling tendencies, and stability evolution within a generalized multi-field context. In practical implementations, however, the operational temperature range must remain below the Curie thresholds of the constituent piezoelectric and piezomagnetic phases in order to preserve magneto–electro–elastic functionality and long-term reliability.

2. Mathematical Formulation

2.1. Geometry and Effective Material Modeling

In this work, a magneto-electro-elastic functionally graded (MEE-FG) nanoplate with an in-plane length L and total thickness is under investigation. The configuration of the structure under investigation is presented in Figure 1. The materials under investigation are composed of a PZT-4/$CoFe_2O_4$ composite system, where PZT-4 represents the piezoelectric constituent of the composite materials under investigation, whereas $CoFe_2O_4$ represents the piezomagnetic constituent of the materials under investigation. The relevant material properties of each constituent are presented in Table 1.

The nanoplate under investigation is subjected to an electric potential field $\Upsilon(x,z,t)$ and a magnetic potential field $\Phi(x,z,t)$. To simulate physically viable changes between the two constituents along the thickness direction, the materials under investigation are assumed to vary continuously rather than discontinuously. This variation can be achieved through a power-law distribution along the thickness direction z.

The volume fraction of the materials under investigation located at the upper surface can be given as follows:

$$V_t(z) = \left(\frac{z}{h}+\frac{1}{2}\right)^p, V_t(z) + V_b(z) = 1, \quad (1)$$

where V_t and V_b denote the thickness-dependent volume fractions of the top and bottom phases, respectively. The exponent p is defined as a material gradient index, which dictates the rate of transition between the two constituents. The z coordinate is measured from the mid-plane of the nanoplate, taking values within the range $[-h/2, h/2]$.

With this gradation, the effective value of an arbitrary material property P at a particular position along the thickness can be represented compactly and analytically as:

$$P(z) = (P_t - P_b)\left(\frac{z}{h} + \frac{1}{2}\right)^p + P_b, \tag{2}$$

where P_t and P_b are defined as the intrinsic properties of the top and bottom constituents, respectively.

This representation provides a smooth and differentiable variation of material properties across the thickness, thus avoiding stiffness matrix discontinuities, which might adversely affect the accuracy of the vibration analysis. As a result, the top surface of the nanoplate, $(z = +h/2)$, is entirely made of $CoFe_2O_4$, while the bottom surface, $(z = -h/2)$, is entirely made of PZT-4. Such a gradual transition allows the coupled electro–magneto–mechanical interactions of both phases to be effectively utilized while maintaining structural stability through the thickness.

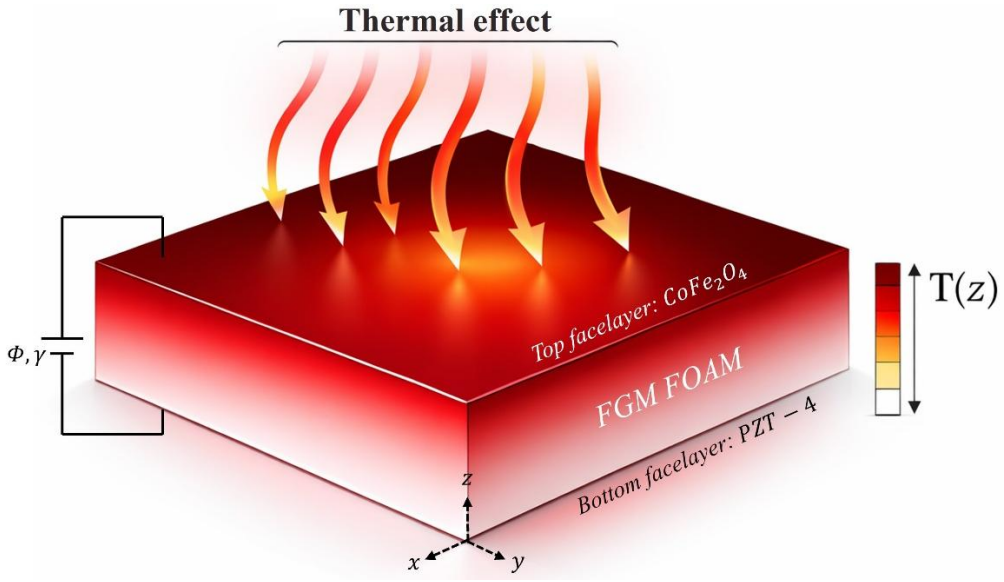

Figure 1. Schematic configuration of the MEE functionally graded nanoplate with face layers under magnetic and thermal fields.

In addition to the through-thickness functional gradation described above, the present study incorporates porosity effects within the MEE–FG nanoplate in order to reflect possible micro-void distributions generated during fabrication. The presence of porosity leads to a reduction in effective stiffness and electromechanical coupling characteristics, and its spatial distribution along the thickness direction may significantly influence the dynamic behavior of the structure. To systematically investigate these effects, three different porosity distribution models are considered, as schematically illustrated in Figure 2.

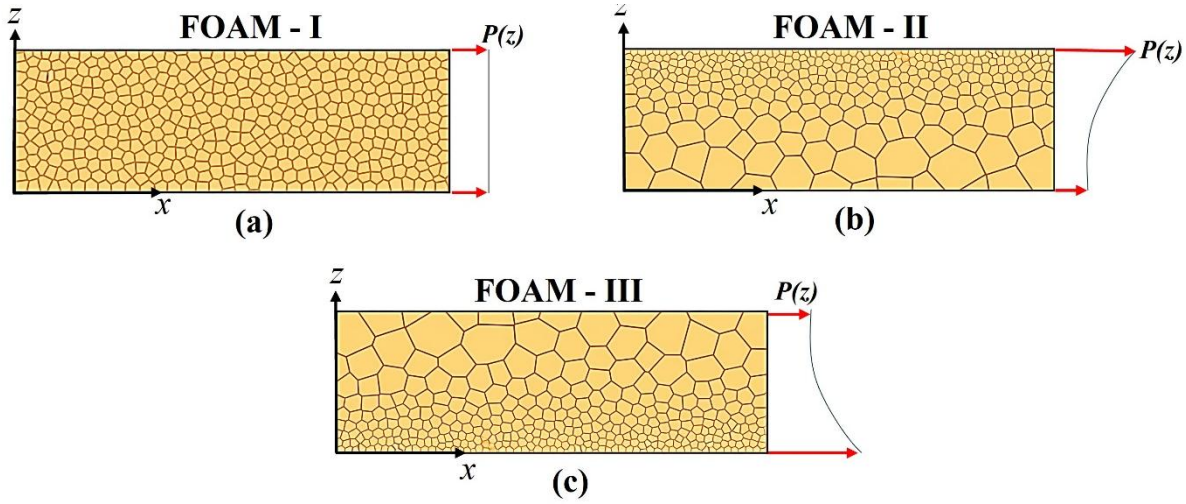

Figure 2. Through-thickness porosity distribution models adopted in the present study: a) Model 1 (uniform); b) Model 2 (bottom-foam); c) Model 3 (top-foam).

Following the schematic representation of the adopted porosity distributions in Figure 2, the porosity effect is incorporated into the present MEE–FG formulation through a thickness-dependent porosity distribution function $\psi_k(z)$, where $k = 1,2,3$ denotes the selected model. In this study, three distinct porosity configurations are considered.

For Foam-I (uniform porosity), the reduction in material properties due to voids is assumed to be constant throughout the thickness, and the porosity function is defined as:

$$\psi_1(z) = 1 - \alpha, \tag{3}$$

where $\alpha \in [0,1]$represents the porosity intensity parameter.

For Foam-II (bottom-foam distribution), in which the porosity is concentrated near the lower surface and gradually decreases toward the upper surface, the distribution function is expressed as:

$$\psi_2(z) = 1 - \alpha\cos\left(\frac{\pi}{2}\left(\frac{z}{h}+\frac{1}{2}\right)\right), \tag{4}$$

whereas for Foam-III (top-foam distribution), characterized by porosity accumulation near the upper surface, the modifier takes the form:

$$\psi_3(z) = 1 - \alpha\cos\left(\frac{\pi}{2}\left(\frac{z}{h}-\frac{1}{2}\right)\right). \tag{5}$$

The above cosine-based definitions ensure a smooth and continuous variation of porosity along the thickness coordinate $z \in [-h/2, h/2]$ without producing non-physical negative values within the admissible parameter range.

To consistently account for both functional gradation and porosity effects, the effective material property at an arbitrary thickness coordinate is obtained by combining the power-law gradation defined in Eq. (2) with the porosity function. Accordingly, the final expression of the thickness-dependent material parameter is written as

$$P(z) = \left[(P_t - P_b)\left(\frac{z}{h}+\frac{1}{2}\right)^p + P_b\right]\psi_k(z), k = 1,2,3. \tag{6}$$

This unified formulation preserves the smooth compositional transition between the PZT-4 and $CoFe_2O_4$ phases while systematically incorporating porosity-induced stiffness degradation into the material description. Consequently, the proposed model enables a consistent evaluation of the coupled effects of gradation index p and porosity intensity α on the electromechanical response of the porous MEE–FG nanoplate.

To accurately account for thermally induced variations in structural response, selected material parameters are treated as temperature-dependent. In the present formulation, the elastic stiffness components C_{ij}, thermal expansion coefficient α, thermal conductivity k, and density $\rho$are modeled as temperature-sensitive quantities. Their variation with temperature is represented

through a nonlinear polynomial expansion that has been widely adopted in thermomechanical modeling of smart composites [53–55].

$$P(T) = P_0(P_{-1}T^{-1}+1+P_1T+P_2T^2+P_3T^3), \tag{7}$$

where P denotes a generic temperature-dependent material parameter evaluated at temperature T (in Kelvin). The coefficients P_{-1}, P_0, P_1, P_2, and P_3 are material-specific constants and are listed in Table 1 for both $CoFe_2O_4$ and PZT-4.

It is emphasized that temperature dependency is introduced only for the properties explicitly provided in Table 1, whereas the remaining electromechanical constants summarized in Table 2 are taken as temperature-invariant within the considered thermal range. Moreover, although the density $\rho(z)$ may exhibit a weak dependence on temperature, its spatial distribution is governed primarily by the through-thickness material gradation.

This modeling strategy captures the essential thermomechanical trends of the FG-MEE nanoplate while keeping the formulation compact and consistent with the temperature-dependent material representation adopted herein.

Table 1 Temperature dependent coefficients for the properties of $CoFe_2O_4$ and PZT-4.

Material	Property	P_{-1}	P_0	P_1	P_2	P_3
$CoFe_2O_4$	C_{11} (Pa)	0	$298.87\text{x}10^9$	$-1.552\text{x}10^{-4}$	$6.125\text{x}10^{-9}$	$-9.0\text{x}10^{-11}$
	C_{55} (Pa)	0	$47.33\text{x}10^9$	$-1.552\text{x}10^{-4}$	$6.125\text{x}10^{-9}$	$-9.0\text{x}10^{-11}$
	υ	0	0.3	0	0	0
	α (1K^{-1})	0	$7.5\text{x}10^{-6}$	$-3.01\text{x}10^{-4}$	$4.02\text{x}10^{-6}$	$-1.01\text{x}10^{-9}$
	κ(W/mK)	0	4.7030	$-1.1\text{x}10^{-3}$	$1.6612\text{x}10^{-6}$	$-9.9670\text{x}10^{-10}$
	ρ (kg/m^3)	0	5300	0	0	0
PZT-4	C_{11} (Pa)	0	$144{,}73\text{x}10^9$	$-1.552\text{x}10^{-4}$	$6.125\text{x}10^{-9}$	$-9.0\text{x}10^{-11}$
	C_{55} (Pa)	0	$26.75\text{x}10^9$	$-1.552\text{x}10^{-4}$	$6.125\text{x}10^{-9}$	$-9.0\text{x}10^{-11}$
	υ	0	0.32	0	0	0
	α (1K^{-1})	0	$1.5\text{x}10^{-6}$	$-3.01\text{x}10^{-4}$	$4.01\text{x}10^{-6}$	$-1.01\text{x}10^{-9}$
	κ(W/mK)	0	2.1	–	–	–
	ρ (kg/m^3)	0	7500	0	0	0

Table 2 Mechanical, electromechanical, and dielectric constants of the face-layer materials at room temperature.

		$CoFe_2O_4$	PZT-4
C_{11}	[GPa]	286	138.5
C_{22}		286	138.5
C_{33}		269.5	114.75
C_{12}		173	77.37
C_{13}		170.5	73.64
C_{23}		170.5	73.64
C_{44}		45.3	25.6
C_{55}		45.3	25.6
C_{66}		56.5	30.6
e_{31}	[C/m^2]	0	-5.2
e_{32}		0	-5.2
e_{33}		0	15.1
ξ_{11}	[$10^{-9}C^2/N.m^2$]	0.08	6.46
ξ_{22}		0.08	6.46
ξ_{33}		0.093	5.62
ρ	[kg/m^3]	5800	7500

2.2. Kinematics and Electromagnetic Field Description

In order to accurately describe the deformation behavior of the MEE-FG nanoplate, a refined higher-order shear deformation plate theory is used. This plate theory is well recognized for the analysis of shear deformable plates and does not require any artificial shear correction factor, as discussed in previous works [56]. In this context, the displacement field of the nanoplate is expressed in terms of the following equations:

$$U(x,y,z,t) = u_0(x,y,t) - z\frac{\partial w_b}{\partial x} - f(z)\frac{\partial w_s}{\partial x}, \tag{8a}$$

$$V(x,y,z,t) = v_0(x,y,t) - z\frac{\partial w_b}{\partial y} - f(z)\frac{\partial w_s}{\partial y}, \tag{8b}$$

$$W(x,y,z,t) = w_b(x,y,t) + w_s(x,y,t), \tag{8c}$$

Here, u_0 and v_0 denote the in-plane displacements of the mid-surface, while $w_b$and $w_s$represent the bending and transverse shear components of the transverse deflection, respectively. In refined plate theories, thickness stretching effects are sometimes considered; however, in this investigation, these effects are ignored based on the plane stress assumption used in this study [57].

The function $f(z)$ represents the thickness-wise variation of transverse shear deformation and facilitates realistic description of the shear deformation response of the nanoplate without

considering any shear correction factor. In this investigation, the function f(z) is selected to be $f(z) = z - \frac{\sin(\zeta z)}{\zeta}$, where ζ is a parameter representing the shear shape function of the nanoplate [56].

Under the quasi-static approximation of Maxwell's equations, the electric and magnetic potentials are assumed to vary through the thickness according to a combined linear–cosine distribution [58]. Accordingly, the electric potential $\Phi$and magnetic potential $\gamma$are written as:

$$\Phi(x, y, z, t) = -\cos(\zeta z)\ \phi(x, y, t) + \frac{2z}{h}V, \tag{9}$$

$$\gamma(x, y, z, t) = \cos(\zeta z)\ \gamma(x, y, t) + \frac{2z}{h}\Omega, \tag{10}$$

where $\zeta = \pi/h$. In these expressions, $V$and Ω denote the externally applied electric voltage and magnetic potential, respectively.

Based on the adopted displacement field, the nonzero strain components of the nanoplate can be written in compact form as:

$$\begin{Bmatrix}\varepsilon_{xx}\\ \varepsilon_{yy}\\ \varepsilon_{xy}\end{Bmatrix} = \begin{Bmatrix}\varepsilon^0_{xx}\\ \varepsilon^0_{yy}\\ \varepsilon^0_{xy}\end{Bmatrix} + z\begin{Bmatrix}k^b_{xx}\\ k^b_{yy}\\ k^b_{xy}\end{Bmatrix} + f(z)\begin{Bmatrix}k^s_{xx}\\ k^s_{yy}\\ k^s_{xy}\end{Bmatrix}, \begin{Bmatrix}\gamma_{xz}\\ \gamma_{yz}\end{Bmatrix} = \begin{Bmatrix}\gamma^0_{xz}\\ \gamma^0_{yz}\end{Bmatrix}, \tag{11}$$

where the mid-plane strains, bending curvatures, shear curvatures, and transverse shear strains are defined as:

$$\begin{pmatrix} \frac{\partial u_0}{} \end{pmatrix} \qquad \begin{pmatrix} -\frac{\partial^2 w_b}{} \end{pmatrix} \tag{12}$$

$$\begin{Bmatrix} k_{xx}^{s} \\ k_{yy}^{s} \\ k_{xy}^{s} \end{Bmatrix} = \begin{Bmatrix} -\dfrac{\partial^2 w_s}{\partial x^2} \\ -\dfrac{\partial^2 w_s}{\partial y^2} \\ -\dfrac{\partial^2 w_s}{\partial x\,\partial y} \end{Bmatrix}, \begin{Bmatrix} \gamma_{xz}^{0} \\ \gamma_{yz}^{0} \end{Bmatrix} = \begin{Bmatrix} \dfrac{\partial w_s}{\partial x} \\ \dfrac{\partial w_s}{\partial y} \end{Bmatrix}.$$

The auxiliary shear function is introduced as:

$$g(z) = 1 - \frac{df(z)}{dz}. \tag{13}$$

The electric field components are obtained from the electric potential as:

$$E_x = -\frac{\partial \Phi}{\partial x} = \cos(\zeta z)\frac{\partial \phi}{\partial x}, \tag{14}$$

$$E_y = -\frac{\partial \Phi}{\partial y} = \cos(\zeta z)\frac{\partial \phi}{\partial y}, \tag{15}$$

$$E_z = -\frac{\partial \Phi}{\partial z} = -\zeta \sin(\zeta z)\,\phi - \frac{2V}{h}, \tag{16}$$

Similarly, the magnetic field components follow from the magnetic potential as:

$$H_x = -\frac{\partial \gamma}{\partial x} = \cos(\zeta z)\frac{\partial \gamma}{\partial x}, \tag{17}$$

$$H_y = -\frac{\partial \gamma}{\partial y} = \cos(\zeta z)\frac{\partial \gamma}{\partial y}, \tag{18}$$

$$H_z = -\frac{\partial \gamma}{\partial z} = -\zeta \sin(\zeta z)\,\gamma - \frac{2\Omega}{h} \tag{19}$$

2.3. Size-Dependent Governing Equations

According to the extended form of Hamilton's principle, the governing equations of the FG-MEE nanoplate are derived from the stationary condition of the total energy functional, comprising the strain energy, the work of external loads, and the kinetic energy:

$$\int_0^t \delta(\Pi_S - \Pi_K + \Pi_W)\, dt = 0 \tag{20}$$

Here, Π_S, Π_W, and Π_K denote the strain energy, external work, and kinetic energy, respectively.

The first variation of the strain energy is expressed in terms of the stress–strain components as:

$$\begin{aligned}\delta\Pi_S = \int_V \left(\sigma_{ij}\, \delta\varepsilon_{ij}\right)\, dV = \int_V \big(&\sigma_{xx}\delta\varepsilon_{xx} + \sigma_{yy}\delta\varepsilon_{yy} + \tau_{xy}\delta\gamma_{xy} + \tau_{yz}\delta\gamma_{yz} + \tau_{xz}\delta\gamma_{xz} - \\ &D_x\delta E_x - D_y\delta E_y - D_z\delta E_z - B_x\delta H_x - B_y\delta H_y - B_z\delta H_z\big)dV\end{aligned} \tag{21}$$

Substituting the previously derived strain–displacement relations into the above expression yields the variational form:

$$\begin{aligned}\delta\Pi_S = &\int_0^L \begin{pmatrix} N_{xx}\dfrac{\partial\delta u_0}{\partial x} - M^b_{xx}\dfrac{\partial^2 w_b}{\partial x^2} - M^s_{xx}\dfrac{\partial^2 w_s}{\partial x^2} + N_{yy}\dfrac{\partial\delta u_0}{\partial y} - M^b_{yy}\dfrac{\partial^2 w_b}{\partial y^2} - M^s_{yy}\dfrac{\partial^2 w_s}{\partial y^2} \\ +N_{xy}\left(\dfrac{\partial u_0}{\partial y} + \dfrac{\partial v_0}{\partial x}\right) - 2M^b_{xy}\dfrac{\partial^2 w_b}{\partial x\partial y} - 2M^s_{xy}\dfrac{\partial^2 w_s}{\partial x\partial y} + Q_{xz}\dfrac{\partial w_s}{\partial x} + Q_{yz}\dfrac{\partial w_s}{\partial y} \end{pmatrix} \mathrm{dx} \\ &+ \int_0^L \int_A \begin{pmatrix} -D_x \cos(\zeta z)\,\delta\left(\dfrac{\partial\phi}{\partial x}\right) - D_y \cos(\zeta z)\,\delta\left(\dfrac{\partial\phi}{\partial y}\right) + D_z \sin(\zeta z)\,\delta\phi \\ -B_x \cos(\zeta z)\,\delta\left(\dfrac{\partial\gamma}{\partial x}\right) - B_y \cos(\zeta z)\,\delta\left(\dfrac{\partial\gamma}{\partial y}\right) + B_z \sin(\zeta z)\,\delta\gamma \end{pmatrix} \mathrm{dAdx}\end{aligned} \tag{22}$$

In the above formulation, the stress resultants are defined through thickness integration as:

$$\left(N_i, M_i^b, M_i^s\right) = \int_A \left(1, z, f(z)\right)\sigma_i\ dA, i = (xx, yy, xy) \tag{23}$$

and the transverse shear resultants are given by:

$$Q_j = \int_A g(z)\sigma_j\ dA, j = (xz, yz) \tag{24}$$

The virtual work corresponding to externally applied in-plane loads takes the form:

$$\begin{aligned}&\delta\Pi_W \\ &= \int_0^L \int_A \begin{pmatrix} N_x^0 \dfrac{\partial(w_b + w_s)}{\partial x}\dfrac{\partial\delta(w_b + w_s)}{\partial x} + N_y^0 \dfrac{\partial(w_b + w_s)}{\partial y}\dfrac{\partial\delta(w_b + w_s)}{\partial y} \\ +2N_{xy}^0 \dfrac{\partial(w_b + w_s)}{\partial x}\dfrac{\partial(w_b + w_s)}{\partial y} \end{pmatrix} dAdx\end{aligned} \tag{25}$$

The variation of the kinetic energy is written as:

$$\delta\Pi_K = \int_V (\dot{U}\delta\dot{U} + \dot{V}\delta\dot{V} + \dot{W}\delta\dot{W})\rho(z)dV$$

$$= \int_0^L \begin{pmatrix} I_0\left(\frac{\partial u_0}{\partial t}\frac{\partial \delta u_0}{\partial t} + \frac{\partial v_0}{\partial t}\frac{\partial \delta v_0}{\partial t} + \frac{\partial (w_b + w_s)}{\partial t}\frac{\partial \delta (w_b + w_s)}{\partial t}\right) \\ -I_1\left(\frac{\partial u_0}{\partial t}\frac{\partial^2 \delta w_b}{\partial x \partial t} + \frac{\partial^2 w_b}{\partial x \partial t}\frac{\partial \delta u_0}{\partial t} + \frac{\partial v_0}{\partial t}\frac{\partial^2 \delta w_b}{\partial y \partial t} + \frac{\partial^2 w_b}{\partial y \partial t}\frac{\partial \delta v_0}{\partial t}\right) \\ -J_1\left(\frac{\partial u_0}{\partial t}\frac{\partial^2 \delta w_s}{\partial x \partial t} + \frac{\partial^2 w_s}{\partial x \partial t}\frac{\partial \delta u_0}{\partial t} + \frac{\partial v_0}{\partial t}\frac{\partial^2 \delta w_s}{\partial y \partial t} + \frac{\partial^2 w_s}{\partial y \partial t}\frac{\partial \delta v_0}{\partial t}\right) \\ +I_2\left(\frac{\partial^2 w_b}{\partial x \partial t}\frac{\partial^2 \delta w_b}{\partial x \partial t} + \frac{\partial^2 w_b}{\partial y \partial t}\frac{\partial^2 \delta w_b}{\partial y \partial t}\right) + K_2\left(\frac{\partial^2 w_s}{\partial x \partial t}\frac{\partial^2 \delta w_s}{\partial x \partial t} + \frac{\partial^2 w_s}{\partial y \partial t}\frac{\partial^2 \delta w_s}{\partial y \partial t}\right) \\ +J_2\left(\frac{\partial^2 w_b}{\partial x \partial t}\frac{\partial^2 \delta w_s}{\partial x \partial t} + \frac{\partial^2 w_s}{\partial x \partial t}\frac{\partial^2 \delta w_b}{\partial x \partial t} + \frac{\partial^2 w_b}{\partial y \partial t}\frac{\partial^2 \delta w_s}{\partial y \partial t} + \frac{\partial^2 w_s}{\partial y \partial t}\frac{\partial^2 \delta w_b}{\partial y \partial t}\right) \end{pmatrix} \mathrm{dx} \tag{26}$$

where the superposed dot denotes differentiation with respect to time. The associated inertia coefficients are defined by:

$$(I_0, I_1, J_1, I_2, J_2, K_2) = \int_A \left(1, z, f(z), z^2, zf(z), f^2(z)\right)\rho(z)\ dA \tag{27}$$

By substituting the above expressions into the stationary condition of the total potential and collecting the coefficients of independent virtual displacements, the Euler–Lagrange equations governing the motion of the MEE–FG nanoplate are obtained as:

$$\frac{\partial N_{xx}}{\partial x} + \frac{\partial N_{xy}}{\partial y} = I_0\frac{\partial^2 u_0}{\partial t^2} - I_1\frac{\partial^3 w_b}{\partial x\,\partial t^2} - J_1\frac{\partial^3 w_s}{\partial x\,\partial t^2} \tag{28}$$

$$\frac{\partial N_{xy}}{\partial x} + \frac{\partial N_{yy}}{\partial y} = I_0\frac{\partial^2 v_0}{\partial t^2} - I_1\frac{\partial^3 w_b}{\partial y\,\partial t^2} - J_1\frac{\partial^3 w_s}{\partial y\,\partial t^2} \tag{29}$$

$$\begin{aligned} &\frac{\partial^2 M_{xx}^b}{\partial x^2} + 2\frac{\partial^2 M_{xy}^b}{\partial x \partial y} + \frac{\partial^2 M_{yy}^b}{\partial y^2} - (N^E + N^H)\nabla^2(w_b + w_s) \\ &\qquad = I_0\frac{\partial^2 (w_b + w_s)}{\partial t^2} + I_1\left(\frac{\partial^3 u_0}{\partial x \partial t^2} + \frac{\partial^3 v_0}{\partial y \partial t^2}\right) - I_2\nabla^2\frac{\partial^2 w_b}{\partial t^2} - J_2\nabla^2\frac{\partial^2 w_s}{\partial t^2} \end{aligned} \tag{30}$$

$$\begin{aligned} &\frac{\partial^2 M_{xx}^s}{\partial x^2} + 2\frac{\partial^2 M_{xy}^s}{\partial x \partial y} + \frac{\partial^2 M_{yy}^s}{\partial y^2} + \frac{\partial Q_{xz}}{\partial x} + \frac{\partial Q_{yz}}{\partial y} - (N^E + N^H)\nabla^2(w_b + w_s) \\ &\qquad = I_0\frac{\partial^2 (w_b + w_s)}{\partial t^2} + J_1\left(\frac{\partial^3 u_0}{\partial x \partial t^2} + \frac{\partial^3 v_0}{\partial y \partial t^2}\right) - J_2\nabla^2\frac{\partial^2 w_b}{\partial t^2} - K_2\nabla^2\frac{\partial^2 w_s}{\partial t^2} \end{aligned} \tag{31}$$

$$\int_A \left(\cos(\zeta z) \frac{\partial D_x}{\partial x} + \cos(\zeta z) \frac{\partial D_y}{\partial y} + \zeta \sin(\zeta z)\, D_z \right) dA = 0 \tag{32}$$

$$\int_A \left(\cos(\zeta z) \frac{\partial B_x}{\partial x} + \cos(\zeta z) \frac{\partial B_y}{\partial y} + \zeta \sin(\zeta z)\, B_z \right) dA = 0 \tag{33}$$

2.4. Nonlocal Strain–Gradient Constitutive Modeling

In the context of the mechanical properties of MEE materials at nanoscale dimensions, it is noted that the classical local theory of elasticity is not sufficient to characterize the mechanical properties of the material, as the stress state not only depends upon the strain at the particular point but also upon the interatomic interaction, as well as the strain variations. In the context of the nonlocal strain gradient theory, the material constitutive relation takes into account the material properties, including the effects of the strain gradient, as well as the effects of the nonlocal interaction. In the context of the mechanical properties of the MEE material, it is noted that the size-dependent theory of the material properties should be considered simultaneously with the effects of the electric field and the magnetic field. In the context of the size-dependent theory of the material properties, the constitutive relation of the material is derived using the differential operator, where the operator is applied to the stress state of the material, as well as the other material properties, so that the material properties can be accurately represented [58].

$$\begin{aligned} &(1-(e_1a)^2\nabla^2)(1-(e_0a)^2\nabla^2)\sigma_{ij} \\ &\quad = (1-(e_1a)^2\nabla^2)\left(C_{ijkl}\varepsilon_{kl} - e_{mij}E_m - q_{nij}H_n\right) \\ &\quad - l^2(1-(e_0a)^2\nabla^2)\left(C_{ijkl}\varepsilon_{kl} - e_{mij}E_m - q_{nij}H_n\right) \end{aligned} \tag{34}$$

$$\begin{aligned} &(1-(e_1a)^2\nabla^2)(1-(e_0a)^2\nabla^2)D_i \\ &\quad = (1-(e_1a)^2\nabla^2)(e_{ikl}\varepsilon_{kl} - s_{im}E_m - d_{in}H_n) \\ &\quad - l^2(1-(e_0a)^2\nabla^2)(e_{ikl}\varepsilon_{kl} - s_{im}E_m - d_{in}H_n) \end{aligned} \tag{35}$$

$$\begin{aligned} &(1-(e_1a)^2\nabla^2)(1-(e_0a)^2\nabla^2)B_i \\ &\quad = (1-(e_1a)^2\nabla^2)\left(q_{ijk}\varepsilon_{kl} - d_{im}E_m - \chi_{in}H_n\right) \\ &\quad - l^2(1-(e_0a)^2\nabla^2)\left(q_{ijk}\varepsilon_{kl} - d_{im}E_m - \chi_{in}H_n\right) \end{aligned} \tag{36}$$

Neglecting the higher-order spatial derivatives of order $O(\nabla^4)$and adopting the commonly employed assumption $e_0 = e_1$, together with the Laplacian definition $\nabla^2 = \partial^2/\partial x^2 + \partial^2/\partial y^2$, the coupled operator expressions can be recast into a reduced and more tractable form as:

$$(1-\mu\nabla^2)\sigma_{ij} = (1-\eta\nabla^2)\left(C_{ijkl}\varepsilon_{kl} - e_{mij}E_m - q_{nij}H_n\right) \tag{37}$$

$$(1-\mu\nabla^2)D_i = (1-\eta\nabla^2)(e_{ikl}\varepsilon_{kl} - s_{im}E_m - d_{in}H_n) \tag{38}$$

$$(1-\mu\nabla^2)B_i = (1-\eta\nabla^2)\left(q_{ijk}\varepsilon_{kl} - d_{im}E_m - \chi_{in}H_n\right) \tag{39}$$

In this formulation, the parameters $\mu = (e_0 a)^2$ and $\eta = l^2$ correspond to the nonlocal interaction coefficient and the intrinsic strain-gradient length-scale parameter, respectively. The former governs the intensity of long-range interatomic effects, whereas the latter characterizes the material's internal resistance associated with higher-order deformation gradients.

Based on these definitions, the constitutive relations of the functionally graded MEE nanoplate can be expressed explicitly in operator form as:

$$(1-\mu\nabla^2)\sigma_{xx} = (1-\eta\nabla^2)\left(\tilde{C}_{11}\varepsilon_{xx} + \tilde{C}_{12}\varepsilon_{yy} - \tilde{e}_{31}E_z - \tilde{q}_{31}H_z\right) \tag{40}$$

$$(1-\mu\nabla^2)\sigma_{yy} = (1-\eta\nabla^2)\left(\tilde{C}_{12}\varepsilon_{xx} + \tilde{C}_{11}\varepsilon_{yy} - \tilde{e}_{31}E_z - \tilde{q}_{31}H_z\right) \tag{41}$$

$$(1-\mu\nabla^2)\sigma_{xy} = (1-\eta\nabla^2)\tilde{C}_{66}\gamma_{xy} \tag{42}$$

$$(1-\mu\nabla^2)\sigma_{xz} = (1-\eta\nabla^2)\left(\tilde{C}_{55}\gamma_{xz} - \tilde{e}_{15}E_x - \tilde{q}_{15}H_x\right) \tag{43}$$

$$(1-\mu\nabla^2)\sigma_{yz} = (1-\eta\nabla^2)\left(\tilde{C}_{55}\gamma_{yz} - \tilde{e}_{15}E_y - \tilde{q}_{15}H_y\right) \tag{44}$$

$$(1-\mu\nabla^2)D_x = (1-\eta\nabla^2)\left(\tilde{e}_{15}\gamma_{xz} + \tilde{s}_{11}E_x - \tilde{d}_{11}H_x\right) \tag{45}$$

$$(1-\mu\nabla^2)D_y = (1-\eta\nabla^2)\left(\tilde{e}_{15}\gamma_{yz} + \tilde{s}_{11}E_y - \tilde{d}_{11}H_y\right) \tag{46}$$

$$(1-\mu\nabla^2)D_z = (1-\eta\nabla^2)\left(\tilde{e}_{31}\varepsilon_{xx} + \tilde{e}_{31}\varepsilon_{yy} + \tilde{s}_{33}E_z - \tilde{d}_{33}H_z\right) \tag{47}$$

$$(1-\mu\nabla^2)B_x = (1-\eta\nabla^2)\left(\tilde{q}_{15}\gamma_{xz} + \tilde{d}_{11}E_x - \tilde{\chi}_{11}H_x\right) \tag{48}$$

$$(1-\mu\nabla^2)B_y=(1-\eta\nabla^2)\left(\tilde{q}_{15}\gamma_{yz}+\tilde{d}_{11}E_y-\tilde{\chi}_{11}H_y\right) \tag{49}$$

$$(1-\mu\nabla^2)B_z=(1-\eta\nabla^2)\left(\tilde{q}_{31}\varepsilon_{xx}+\tilde{q}_{31}\varepsilon_{yy}+\tilde{d}_{33}E_z-\tilde{\chi}_{33}H_z\right) \tag{50}$$

Under the plane-stress assumption, the effective reduced material coefficients of the FG–MEE nanoplate can be obtained by eliminating the out-of-plane stress components and rewriting the coupled constitutive tensors in terms of in-plane quantities. Accordingly, the modified elastic, piezoelectric, and piezomagnetic parameters are expressed as:

$$\begin{gathered}\tilde{C}_{11}=C_{11}-\frac{C_{13}^2}{C_{33}},\quad \tilde{s}_{11}=s_{11},\quad \tilde{e}_{31}=e_{31}-\frac{C_{13}e_{33}}{C_{33}},\quad \tilde{q}_{31}=q_{31}-\frac{C_{13}q_{33}}{C_{33}}\\ \tilde{d}_{11}=d_{11},\quad \tilde{\chi}_{11}=\chi_{11},\quad \tilde{d}_{33}=d_{33}-\frac{e_{33}q_{33}}{C_{33}},\quad \tilde{s}_{33}=s_{33}-\frac{e_{33}^2}{C_{33}}\\ \tilde{s}_{33}=s_{33}-\frac{e_{33}^2}{C_{33}}\end{gathered} \tag{51}$$

Subsequently, by integrating the size-dependent constitutive relations through the plate thickness, the membrane force–strain and bending moment–curvature relations of the nonlocal refined FG–MEE nanoplate are derived in operator form as:

$$\begin{gathered}(1-\mu\nabla^2)\begin{Bmatrix}N_{xx}\\N_{yy}\\N_{xy}\end{Bmatrix}=(1-\eta\nabla^2)\\ \begin{pmatrix}A_{11}&A_{12}&0\\A_{21}&A_{22}&0\\0&0&A_{66}\end{pmatrix}\begin{Bmatrix}\dfrac{\partial u_0}{\partial x}\\[2mm]\dfrac{\partial v_0}{\partial y}\\[2mm]\dfrac{\partial u_0}{\partial y}+\dfrac{\partial v_0}{\partial x}\end{Bmatrix}+\begin{pmatrix}B_{11}&B_{12}&0\\B_{21}&B_{22}&0\\0&0&B_{66}\end{pmatrix}\begin{Bmatrix}-\dfrac{\partial^2 w_b}{\partial x^2}\\[2mm]-\dfrac{\partial^2 w_b}{\partial y^2}\\[2mm]-2\dfrac{\partial^2 w_b}{\partial x\partial y}\end{Bmatrix}+\\ \begin{pmatrix}B_{11}^s&B_{12}^s&0\\B_{21}^s&B_{22}^s&0\\0&0&B_{66}^s\end{pmatrix}\begin{Bmatrix}-\dfrac{\partial^2 w_s}{\partial x^2}\\[2mm]-\dfrac{\partial^2 w_s}{\partial y^2}\\[2mm]-2\dfrac{\partial^2 w_s}{\partial x\partial y}\end{Bmatrix}+\begin{pmatrix}A_{31}^e\\A_{31}^e\\0\end{pmatrix}\phi+\begin{pmatrix}A_{31}^m\\A_{31}^m\\0\end{pmatrix}\gamma-\begin{pmatrix}N_x^E+N_x^H\\N_y^E+N_y^H\\0\end{pmatrix}\end{gathered} \tag{52}$$

$$(1-\mu\nabla^2)\begin{Bmatrix} M_{xx}^b \\ M_{yy}^b \\ M_{xy}^b \end{Bmatrix} = (1-\eta\nabla^2)$$

$$\begin{pmatrix} B_{11} & B_{12} & 0 \\ B_{21} & B_{22} & 0 \\ 0 & 0 & B_{66} \end{pmatrix}\begin{Bmatrix} \dfrac{\partial u_0}{\partial x} \\ \dfrac{\partial v_0}{\partial y} \\ \dfrac{\partial u_0}{\partial y}+\dfrac{\partial v_0}{\partial x} \end{Bmatrix} + \begin{pmatrix} D_{11} & D_{12} & 0 \\ D_{21} & D_{22} & 0 \\ 0 & 0 & D_{66} \end{pmatrix}\begin{Bmatrix} -\dfrac{\partial^2 w_b}{\partial x^2} \\ -\dfrac{\partial^2 w_b}{\partial y^2} \\ -2\dfrac{\partial^2 w_b}{\partial x \partial y} \end{Bmatrix} + \tag{53}$$

$$\begin{pmatrix} D_{11}^s & D_{12}^s & 0 \\ D_{21}^s & D_{22}^s & 0 \\ 0 & 0 & D_{66}^s \end{pmatrix}\begin{Bmatrix} -\dfrac{\partial^2 w_s}{\partial x^2} \\ -\dfrac{\partial^2 w_s}{\partial y^2} \\ -2\dfrac{\partial^2 w_s}{\partial x \partial y} \end{Bmatrix} + \begin{pmatrix} E_{31}^e \\ E_{31}^e \\ 0 \end{pmatrix}\phi + \begin{pmatrix} E_{31}^m \\ E_{31}^m \\ 0 \end{pmatrix}\gamma - \begin{pmatrix} M_{bx}^E + M_{bx}^H \\ M_{by}^E + M_{by}^H \\ 0 \end{pmatrix}$$

$$(1-\mu\nabla^2)\begin{Bmatrix} M_{xx}^s \\ M_{yy}^s \\ M_{xy}^s \end{Bmatrix} = (1-\eta\nabla^2)$$

$$\left(\begin{pmatrix} B_{11}^s & B_{12}^s & 0 \\ B_{21}^s & B_{22}^s & 0 \\ 0 & 0 & B_{66}^s \end{pmatrix}\begin{Bmatrix} \dfrac{\partial u_0}{\partial x} \\ \dfrac{\partial v_0}{\partial y} \\ \dfrac{\partial u_0}{\partial y}+\dfrac{\partial v_0}{\partial x} \end{Bmatrix} + \begin{pmatrix} D_{11}^s & D_{12}^s & 0 \\ D_{21}^s & D_{22}^s & 0 \\ 0 & 0 & D_{66}^s \end{pmatrix}\begin{Bmatrix} -\dfrac{\partial^2 w_b}{\partial x^2} \\ -\dfrac{\partial^2 w_b}{\partial y^2} \\ -2\dfrac{\partial^2 w_b}{\partial x \partial y} \end{Bmatrix} + \right. \tag{54}$$

$$\left. \begin{pmatrix} H_{11}^s & H_{12}^s & 0 \\ H_{21}^s & H_{22}^s & 0 \\ 0 & 0 & H_{66}^s \end{pmatrix}\begin{Bmatrix} -\dfrac{\partial^2 w_s}{\partial x^2} \\ -\dfrac{\partial^2 w_s}{\partial y^2} \\ -2\dfrac{\partial^2 w_s}{\partial x \partial y} \end{Bmatrix} + \begin{pmatrix} F_{31}^e \\ F_{31}^e \\ 0 \end{pmatrix}\phi + \begin{pmatrix} F_{31}^m \\ F_{31}^m \\ 0 \end{pmatrix}\gamma - \begin{pmatrix} M_{sx}^E + M_{sx}^H \\ M_{sy}^E + M_{sy}^H \\ 0 \end{pmatrix} \right)$$

$$(1-\mu\nabla^2)\begin{Bmatrix} Q_{xz} \\ Q_{yz} \end{Bmatrix} = (1-\eta\nabla^2)\left(\begin{pmatrix} A_{44}^s & 0 \\ 0 & A_{55}^s \end{pmatrix}\begin{Bmatrix} \dfrac{\partial w_s}{\partial x} \\ \dfrac{\partial w_s}{\partial y} \end{Bmatrix} \right. \tag{55}$$

$$\left. -A_{15}^e\begin{Bmatrix} \dfrac{\partial \phi}{\partial x} \\ \dfrac{\partial \phi}{\partial y} \end{Bmatrix} - A_{15}^m\begin{Bmatrix} \dfrac{\partial \gamma}{\partial x} \\ \dfrac{\partial \gamma}{\partial y} \end{Bmatrix} \right)$$

$$\int_A \left((1-\mu\nabla^2) \begin{Bmatrix} D_x \\ D_y \end{Bmatrix} \cos(\zeta z) \right) \mathrm{dA} = (1-\eta\nabla^2) \left(E_{15}^e \begin{Bmatrix} \frac{\partial w_s}{\partial x} \\ \frac{\partial w_s}{\partial y} \end{Bmatrix} - F_{11}^e \begin{Bmatrix} \frac{\partial \phi}{\partial x} \\ \frac{\partial \phi}{\partial y} \end{Bmatrix} - F_{11}^m \begin{Bmatrix} \frac{\partial \gamma}{\partial x} \\ \frac{\partial \gamma}{\partial y} \end{Bmatrix} \right) \tag{56}$$

$$\int_A \left((1-\mu\nabla^2) D_z \zeta \sin(\zeta z) \right) \mathrm{dA} = (1-\eta\nabla^2) \left(A_{31}^e \left(\frac{\partial u_0}{\partial x} + \frac{\partial v_0}{\partial y} \right) - E_{31}^e \nabla^2 w_b - F_{31}^e \nabla^2 w_s - F_{33}^e \phi - F_{33}^m \gamma \right) \tag{57}$$

$$\int_A \left((1-\mu\nabla^2) \begin{Bmatrix} B_x \\ B_y \end{Bmatrix} \cos(\zeta z) \right) \mathrm{dA} = (1-\eta\nabla^2) \left(E_{15}^m \begin{Bmatrix} \frac{\partial w_s}{\partial x} \\ \frac{\partial w_s}{\partial y} \end{Bmatrix} - F_{11}^m \begin{Bmatrix} \frac{\partial \phi}{\partial x} \\ \frac{\partial \phi}{\partial y} \end{Bmatrix} - X_{11}^m \begin{Bmatrix} \frac{\partial \gamma}{\partial x} \\ \frac{\partial \gamma}{\partial y} \end{Bmatrix} \right) \tag{58}$$

$$\int_A \left((1-\mu\nabla^2) B_z \zeta \sin(\zeta z) \right) \mathrm{dA} = (1-\eta\nabla^2) \left(A_{31}^m \left(\frac{\partial u_0}{\partial x} + \frac{\partial v_0}{\partial y} \right) - E_{31}^m \nabla^2 w_b - F_{31}^m \nabla^2 w_s - F_{33}^m \phi - X_{33}^m \gamma \right) \tag{59}$$

The sectional stiffness coefficients appearing in the above operator equations are introduced below in explicit integral form:

$$\begin{pmatrix} A_{11} & B_{11} & D_{11} & B_{11}^s & D_{11}^s & H_{11}^s \\ A_{12} & B_{12} & D_{12} & B_{12}^s & D_{12}^s & H_{12}^s \\ A_{66} & B_{66} & D_{66} & B_{66}^s & D_{66}^s & H_{66}^s \end{pmatrix} = \int_A \left(\left(1, z, z^2, f(z), zf(z), f^2(z)\right) \begin{Bmatrix} \tilde{c}_{11} \\ \tilde{c}_{12} \\ \tilde{c}_{66} \end{Bmatrix} \right) \mathrm{dA} \tag{60}$$

$$(A_{31}^e, E_{31}^e, F_{31}^e) = \int_A \left(1, z, f(z)\right) \tilde{e}_{31} \zeta \sin(\zeta z)\, \mathrm{dA} \tag{61}$$

$$(A_{31}^m, E_{31}^m, F_{31}^m) = \int_A \left(1, z, f(z)\right) \tilde{q}_{31} \zeta \sin(\zeta z)\, \mathrm{dA} \tag{62}$$

$$(A_{15}^{e}, E_{15}^{e}) = \int_{A} \big(1, g(z)\big)\tilde{e}_{31}\cos(\zeta z)\,\mathrm{dA} \tag{63}$$

$$(A_{15}^{m}, E_{15}^{m}) = \int_{A} \big(1, g(z)\big)\tilde{q}_{31}\cos(\zeta z)\,\mathrm{dA} \tag{64}$$

$$(F_{11}^{e}, F_{33}^{e}) = \int_{A} (\tilde{s}_{11}\cos^2(\zeta z), \tilde{s}_{33}\zeta^2\sin^2(\zeta z))\mathrm{dA} \tag{65}$$

$$(F_{11}^{m}, F_{33}^{m}) = \int_{A} \big(\tilde{d}_{11}\cos^2(\zeta z), \tilde{d}_{33}\zeta^2\sin^2(\zeta z)\big)\mathrm{dA} \tag{66}$$

$$(X_{11}^{m}, X_{33}^{m}) = \int_{A} (\tilde{\chi}_{11}\cos^2(\zeta z), \tilde{\chi}_{33}\zeta^2\sin^2(\zeta z))\mathrm{dA} \tag{67}$$

$$(A_{44}^{s}, A_{55}^{s}) = \int_{A} \big(\tilde{q}_{44}g^2(z)\big)\mathrm{dA} \tag{68}$$

Applied electro-magnetic actuation generates additional in-plane force resultants and bending moments in the FG–MEE nanoplate, which are incorporated into the membrane–bending relations given in Eqs. (51)–(53). The electrically and magnetically induced in-plane forces can therefore be expressed as:

$$N_x^E = N_y^E = -\int_A \left(\tilde{e}_{31}\frac{2V}{h}\right)dA, \qquad N_x^H = N_y^H = -\int_A \left(\tilde{q}_{31}\frac{2\Omega}{h}\right)dA \tag{69}$$

Similarly, the bending moments associated with the electric and magnetic potentials take the form:

$$M_{bx}^E = M_{by}^E = -\int_A \left(\tilde{e}_{31}\frac{2V}{h}z\right)dA, \qquad M_{bx}^H = M_{by}^H = -\int_A \left(\tilde{q}_{31}\frac{2\Omega}{h}z\right)dA \tag{70}$$

and the corresponding shear-related moment components are given by:

$$M_{sx}^E = M_{sy}^E = -\int_A \left(\tilde{e}_{31}\frac{2V}{h}f(z)\right)dA, \quad M_{sx}^H = M_{sy}^H = -\int_A \left(\tilde{q}_{31}\frac{2V}{h}f(z)\right)dA \tag{71}$$

The thermal force resultants associated with each layer are evaluated through the following integral expressions [59]:

$$N_x^T = b\int_{-\frac{h}{2}-h_p}^{-\frac{h}{2}} c_{face11}\alpha_{face}\Delta T + \int_{-\frac{h}{2}}^{\frac{h}{2}} c_{core11}\alpha_{core}\Delta T \int_{\frac{h}{2}}^{\frac{h}{2}+h_p} c_{face11}\alpha_{face}\Delta T \tag{72a}$$

$$N_y^T = a\int_{-\frac{h}{2}-h_p}^{-\frac{h}{2}} c_{face11}\alpha_{face}\Delta T + \int_{-\frac{h}{2}}^{\frac{h}{2}} c_{core11}\alpha_{core}\Delta T \int_{\frac{h}{2}}^{\frac{h}{2}+h_p} c_{face11}\alpha_{face}\Delta T \tag{72b}$$

In this expressions, c_{face11}, and c_{core11} denote the effective elastic coefficients of the face and core layers, respectively. The parameters, α_{face}, and α_{core} correspond to the thermal expansion coefficients of the face and core regions, as reported in [10,33]. Considering the square geometry of the nanoplate, the thermal force resultants reduce to $N_x^T = N_y^T = N^T$.

Finally, by substituting Eqs. (51)–(58) together with Eqs. (69)–(71) into the governing relations provided in Eqs. (28)–(33), the resulting nonlocal equations of motion of the FG–MEE nanoplate can be formulated directly in terms of the displacement variables.

$$\begin{aligned}(1-\eta\nabla^2)\Bigg(&A_{11}\frac{\partial^2 u_0}{\partial x^2}+(A_{12}+A_{66})\frac{\partial^2 v_0}{\partial x\partial y}+A_{66}\frac{\partial^2 u_0}{\partial y^2}-B_{11}\frac{\partial^3 w_b}{\partial x^3}-(B_{12}+2B_{66})\frac{\partial^3 w_b}{\partial x\partial y^2}\\ &-B_{11}^s\frac{\partial^3 w_s}{\partial x^3}-(B_{12}^s+2B_{66}^s)\frac{\partial^3 w_s}{\partial x\partial y^2}+A_{31}^e\frac{\partial\phi}{\partial x}+A_{31}^m\frac{\partial\gamma}{\partial x}\Bigg)\\ &+(1-\mu\nabla^2)\left(-I_0\frac{\partial^2 u_0}{\partial t^2}+I_1\frac{\partial^3 w_b}{\partial x\partial t^2}+J_1\frac{\partial^3 w_s}{\partial x\partial t^2}\right)=0\end{aligned} \tag{73}$$

$$\begin{aligned}(1-\eta\nabla^2)\Bigg(&A_{22}\frac{\partial^2 v_0}{\partial y^2}+(A_{12}+A_{66})\frac{\partial^2 u_0}{\partial x\partial y}+A_{66}\frac{\partial^2 v_0}{\partial x^2}-B_{22}\frac{\partial^3 w_b}{\partial y^3}-(B_{12}+2B_{66})\frac{\partial^3 w_b}{\partial x^2\partial y}\\ &-B_{22}^s\frac{\partial^3 w_s}{\partial y^3}-(B_{12}^s+2B_{66}^s)\frac{\partial^3 w_s}{\partial x^2\partial y}+A_{31}^e\frac{\partial\phi}{\partial y}+A_{31}^m\frac{\partial\gamma}{\partial y}\Bigg)\\ &+(1-\mu\nabla^2)\left(-I_0\frac{\partial^2 v_0}{\partial t^2}+I_1\frac{\partial^3 w_b}{\partial y\partial t^2}+J_1\frac{\partial^3 w_s}{\partial y\partial t^2}\right)=0\end{aligned} \tag{74}$$

$$\begin{aligned}(1-\eta\nabla^2)\Bigg(&B_{11}\frac{\partial^3 u_0}{\partial x^3}+(B_{12}+2B_{66})\frac{\partial^3 u_0}{\partial x\partial y^2}+B_{22}\frac{\partial^3 v_0}{\partial y^3}+(B_{12}+2B_{66})\frac{\partial^3 v_0}{\partial x^2\partial y}\\ &-D_{11}\frac{\partial^4 w_b}{\partial x^4}-2(D_{12}+2D_{66})\frac{\partial^4 w_b}{\partial x^2\partial y^2}-D_{22}\frac{\partial^4 w_b}{\partial y^4}+E_{31}^e\nabla^2\phi\\ &-D_{11}^S\frac{\partial^4 w_s}{\partial x^4}-2\left(D_{12}^S+2D_{66}^S\right)\frac{\partial^4 w_s}{\partial x^2\partial y^2}-D_{22}^S\frac{\partial^4 w_s}{\partial y^4}+E_{31}^m\nabla^2\gamma\Bigg)\\ +(1-\mu\nabla^2)\Bigg(&-I_0\frac{\partial^2(w_b+w_s)}{\partial t^2}-I_1\left(\frac{\partial^3 u_0}{\partial x\partial t^2}+\frac{\partial^3 v_0}{\partial y\partial t^2}\right)+I_2\nabla^2\frac{\partial^2 w_b}{\partial t^2}\\ &+J_2\nabla^2\frac{\partial^2 w_s}{\partial t^2}-(N^E+N^T)\nabla^2(w_b+w_s)\Bigg)=0\end{aligned} \tag{75}$$

$$(1-\eta\nabla^2)\begin{pmatrix} B_{11}^s\frac{\partial^3 u_0}{\partial x^3}+(B_{12}^s+2B_{66}^s)\frac{\partial^3 u_0}{\partial x\partial y^2}+B_{22}^s\frac{\partial^3 v_0}{\partial y^3}+(B_{12}^s+2B_{66}^s)\frac{\partial^3 v_0}{\partial x^2\partial y} \\ -D_{11}^s\frac{\partial^4 w_b}{\partial x^4}-2(D_{12}^s+2D_{66}^s)\frac{\partial^4 w_b}{\partial x^2\partial y^2}-D_{22}^s\frac{\partial^4 w_b}{\partial y^4}+(F_{31}^e-E_{15}^e)\nabla^2\phi- \\ H_{11}^s\frac{\partial^4 w_s}{\partial x^4}-2(H_{12}^s+2H_{66}^s)\frac{\partial^4 w_s}{\partial x^2\partial y^2}-H_{22}^s\frac{\partial^4 w_s}{\partial y^4}+(F_{31}^m-E_{15}^m)\nabla^2\gamma+A_{44}^s\nabla^2 w_s \end{pmatrix} \quad (76)$$
$$+(1-\mu\nabla^2)\begin{pmatrix} -I_0\frac{\partial^2(w_b+w_s)}{\partial t^2}-J_1\left(\frac{\partial^3 u_0}{\partial x\partial t^2}+\frac{\partial^3 v_0}{\partial y\partial t^2}\right)+J_2\nabla^2\frac{\partial^2 w_b}{\partial t^2} \\ +K_2\nabla^2\frac{\partial^2 w_s}{\partial t^2}-(N^E+N^T)\nabla^2(w_b+w_s) \end{pmatrix}=0$$

$$(1-\eta\nabla^2)\begin{pmatrix} A_{31}^e\left(\frac{\partial u_0}{\partial x}+\frac{\partial v_0}{\partial y}\right)-E_{31}^e\nabla^2 w_b-(F_{31}^e-E_{15}^e)\nabla^2 w_s \\ +F_{11}^e\nabla^2\phi+F_{11}^m\nabla^2\gamma-F_{33}^e\phi-F_{33}^m\gamma \end{pmatrix}=0 \quad (77)$$

$$(1-\eta\nabla^2)\begin{pmatrix} A_{31}^m\left(\frac{\partial u_0}{\partial x}+\frac{\partial v_0}{\partial y}\right)-E_{31}^m\nabla^2 w_b-(F_{31}^m-E_{15}^m)\nabla^2 w_s \\ +F_{11}^m\nabla^2\phi+X_{11}^m\nabla^2\gamma-F_{33}^m\phi-X_{33}^m\gamma \end{pmatrix}=0 \quad (78)$$

The FG–MEE nanoplate is assumed to be subjected to externally applied electric voltage and magnetic potential, while transverse shear loading is neglected in the present formulation. Under these conditions, the in-plane shear force resultant satisfies $N_{xy}=0$. Accordingly, the normal in-plane force components induced by the applied electro–magnetic fields can be written as:

$$N_x^0=N_y^0=N^E+N^T$$
$$N^E=-\int_A\left(\tilde{e}_{31}\frac{2V}{h}\right)dA,\quad N^T=-\int_A\left(\tilde{q}_{31}\frac{2\Omega}{h}\right)dA \quad (79)$$

3. Analytical Solution

In this section, the previously established nonlocal governing equations are solved analytically. To investigate the wave propagation characteristics of the FG–MEE nanoplate, the mechanical displacements and electric–magnetic potentials are assumed to follow harmonic exponential distributions of the form:

$$\begin{Bmatrix} u_0(x,y,t) \\ v_0(x,y,t) \\ w_b(x,y,t) \\ w_s(x,y,t) \\ \phi(x,y,t) \\ \gamma(x,y,t) \end{Bmatrix} = \begin{Bmatrix} U\exp\left[i(k_1x + k_2y - \omega t)\right] \\ V\exp\left[i(k_1x + k_2y - \omega t)\right] \\ W_b\exp\left[i(k_1x + k_2y - \omega t)\right] \\ W_s\exp\left[i(k_1x + k_2y - \omega t)\right] \\ \phi\exp\left[i(k_1x + k_2y - \omega t)\right] \\ \Upsilon\exp\left[i(k_1x + k_2y - \omega t)\right] \end{Bmatrix} \tag{80}$$

where U, V, W_b, W_s, Φ, and Υ denote the unknown amplitude parameters. The quantities $k_1$and $k_2$represent the wave numbers associated with the propagation directions along the x- and y-axes, respectively, and ω is the circular frequency of the propagating wave.

Substituting Eq. (80) into Eqs. (73)–(78) yields the following eigenvalue problem:

$$([K]_{6\times6} - \omega^2[M]_{6\times6})\{\Delta\} = \{0\} \tag{81}$$

The vector of unknown generalized amplitudes appearing in Eq. (81) is defined as:

$$\{\Delta\} = \{U, V, W_b, W_s, \phi, \Upsilon\}^T \tag{82}$$

The explicit forms of the stiffness and mass matrices, whose elements are functions of the sectional rigidity coefficients and inertia terms, are provided in Appendix. The dispersion relation governing the wave propagation characteristics of the system is obtained by enforcing the vanishing determinant condition:

$$|[K]_{6\times6} - \omega^2[M]_{6\times6}| = 0 \tag{83}$$

The detailed matrix components of $[K]$and $[M]$ are presented in Appendix.

4. Results and Discussion

4.1 Effect of Porosity Distribution and Material Gradation

Figures 3 and 4 illustrate the impact of the porosity index and the distribution pattern on the dimensionless fundamental frequency parameter λ_{11} for varying temperature rises and distinct configurations of the porous functionally graded medium. As the porosity index increases, the dimensionless fundamental frequency parameter λ_{11} decreases, regardless of the model of the porous functionally graded medium used in the analysis. This phenomenon is attributed to the degradation in the effective stiffness, resulting in the degradation of the load-bearing capacity of the functionally graded medium due to the increasing volume fraction of the voids. However, the rate at which the dimensionless fundamental frequency parameter λ_{11} is affected by the

porosity index is highly dependent on the distribution pattern used in the analysis. Of the configurations used in the analysis, FOAM I is found to have the maximum degradation in the effective stiffness, resulting in the early tendency towards zero frequency at higher porosity levels, even at lower temperature rises. On the contrary, FOAM II and FOAM III have relatively smoother degradation in the dimensionless fundamental frequency parameter λ_{11}, signifying the balanced degradation in the effective stiffness in the direction of the thickness.

Moreover, the impact of the material gradation index p is found to modulate the response of the dimensionless fundamental frequency parameter λ_{11}, where the material gradation index is found to result in the degradation in the effective stiffness due to the degradation in the material properties, where the material properties tend towards the properties of the compliant material over the entire range of the thickness due to the increased value of the gradation index p. This phenomenon is found to have been highlighted in Figure 4, where the impact of the porosity index is found to have been amplified at higher temperature rises, resulting in the degradation in the dimensionless fundamental frequency parameter λ_{11}. The degradation in the dimensionless fundamental frequency parameter λ_{11} is found to result in the degradation in the effective stiffness, leading the structure towards instability due to the in-plane compressive stresses, resulting in the decrease in the dimensionless fundamental frequency parameter λ_{11} with the increase in the temperature rise ΔT. Moreover, the impact of the porosity index is found to have been more significant at higher temperature rises, signifying the role of the porosity distribution in the determination of the thermo-vibrational stability of the porous functionally graded medium.

The overall findings suggest that the dynamic response of porous functionally graded MEE nanoplates depends on the combined influence of porosity level, its distribution pattern, and the gradation profile of the materials used. Therefore, an optimal design of the porosity distribution pattern can effectively alleviate the extent of stiffness degradation and the onset of thermal-induced frequency collapse.

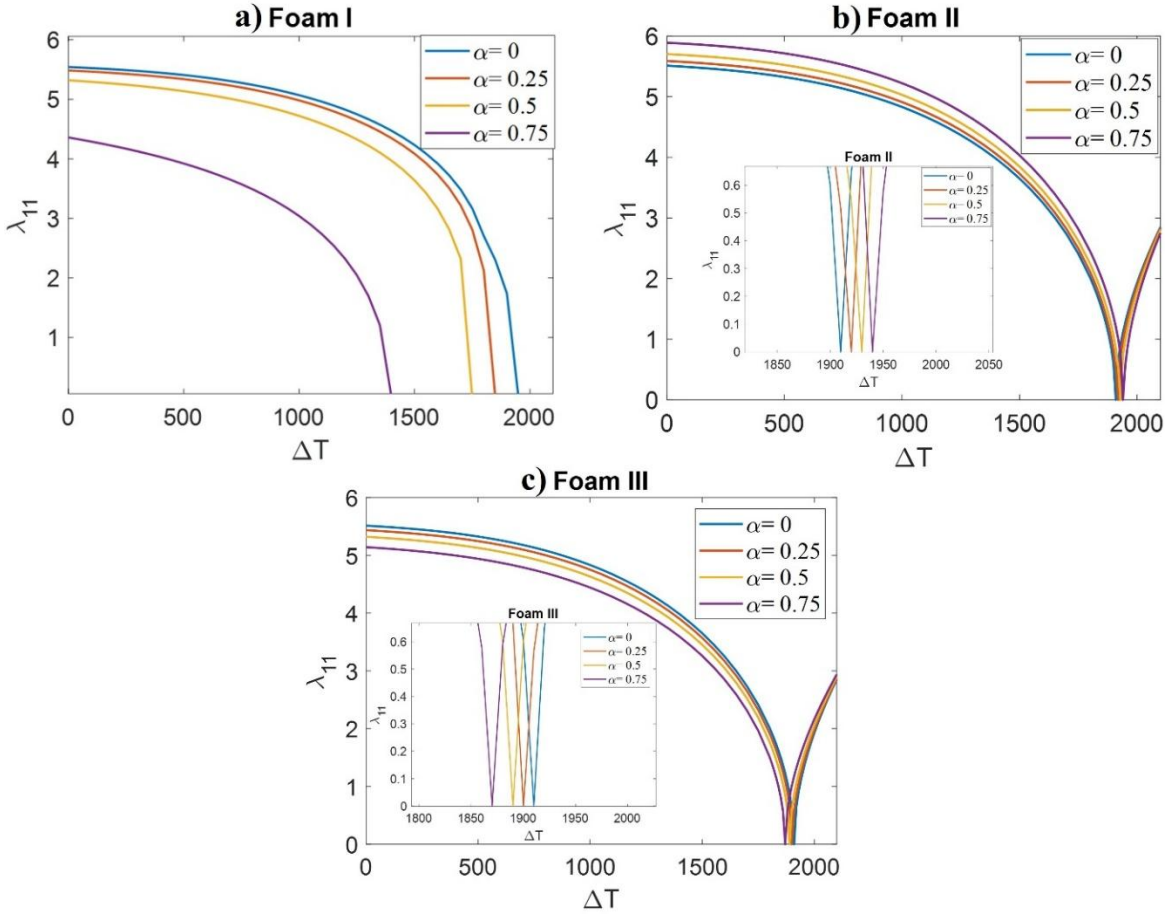

Figure 3. Comparison of the variation of the dimensionless fundamental frequency parameter λ_{11} with porosity index $\alpha = 0,0.25,0.5,0.75$for material gradation index $p = 1$; aspect ratio $h = a/10$; electric potential parameter $V_m = 0$; magnetic potential parameter $H_m = 0$; nonlocal parameter $e_0 a = 0$; material length scale parameter $l_m = 0$. (a) FOAM I; (b) FOAM II; (c) FOAM III.

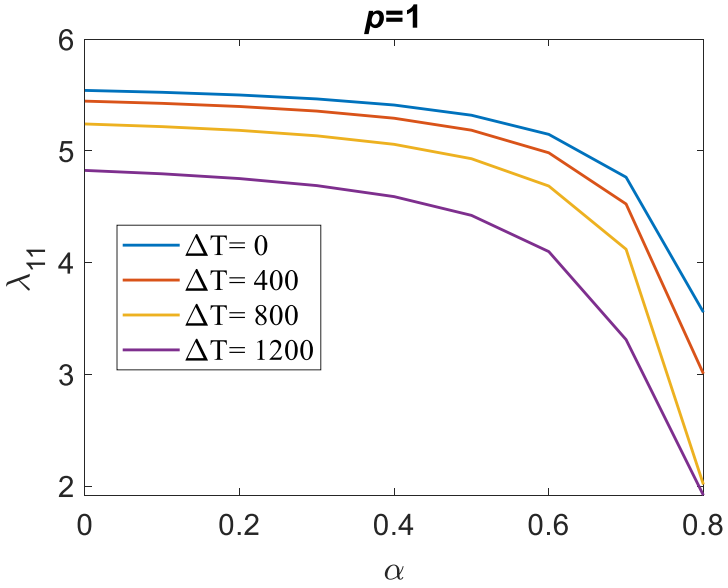

Figure 4. Variation of the dimensionless fundamental frequency parameter $\lambda_{11}$with porosity index $\alpha$for different temperature rises $\Delta T = 0,400,800,1200$; aspect ratio $h = a/10$; material gradation index $p = 1$; electric potential parameter $V_m = 0$; magnetic potential parameter $H_m = 0$.

4.2 Effect of Temperature Rise

Figures 5 and 6 show the variation of the dimensionless fundamental natural frequency parameter λ_{11} with an increase in temperature rise ΔT for different gradation indices and porosity patterns. The dimensionless fundamental natural frequency parameter λ_{11} shows a monotonic decrease with an increase in ΔT for different gradation indices and porosity patterns. This indicates that the nanoplates are more prone to thermal-induced stiffness degradation with an increase in ΔT.

The variation of the dimensionless fundamental natural frequency parameter λ_{11} with an increase in ΔT for the porous nanoplates ($\alpha = 0.7$) shows that the sensitivity of the fundamental natural frequency parameter to an increase in ΔT depends on the gradation index of the materials used in the nanoplates. Lower values of the gradation index p show higher values of λ_{11} compared to higher values of the gradation index used in the nanoplates. This indicates that nanoplates with a higher volume fraction of the stiffer materials used in the nanoplates are more resistant to thermal-induced stiffness degradation compared to nanoplates with higher values of the gradation index used in the nanoplates. FOAM I shows a higher rate of decrease in the dimensionless fundamental natural frequency parameter λ_{11} compared to FOAM II and FOAM III nanoplates. This indicates that the distribution pattern used in FOAM I nanoplates accelerates the extent of stiffness degradation under thermal loading compared to FOAM II and FOAM III nanoplates.

A comparative evaluation in terms of the solid configuration, i.e., $\alpha = 0$, reveals the overall impact of porosity and temperature. It is observed that, although there is a reduction in frequency in the case of the nanoplate in the solid configuration, there is a rapid reduction in frequency at a higher temperature level in comparison to other porous configurations. It can therefore be concluded that porosity not only reduces the baseline stiffness of the nanoplate, but there is also an overall increase in thermally induced softening effects. Hence, porous FG-MEE nanoplates are found to attain thermally induced instability at a faster rate in comparison to nanoplates in the solid configuration.

In summary, it can be stated that there is a significant impact of temperature rise as a destabilizing factor in the dynamic response of FG-MEE nanoplates. The impact is found to increase with gradation index values and porosity levels. The incorporation of temperature-dependent material properties and thermally developed in-plane forces is therefore essential in accurately modeling the size-dependent vibration response.

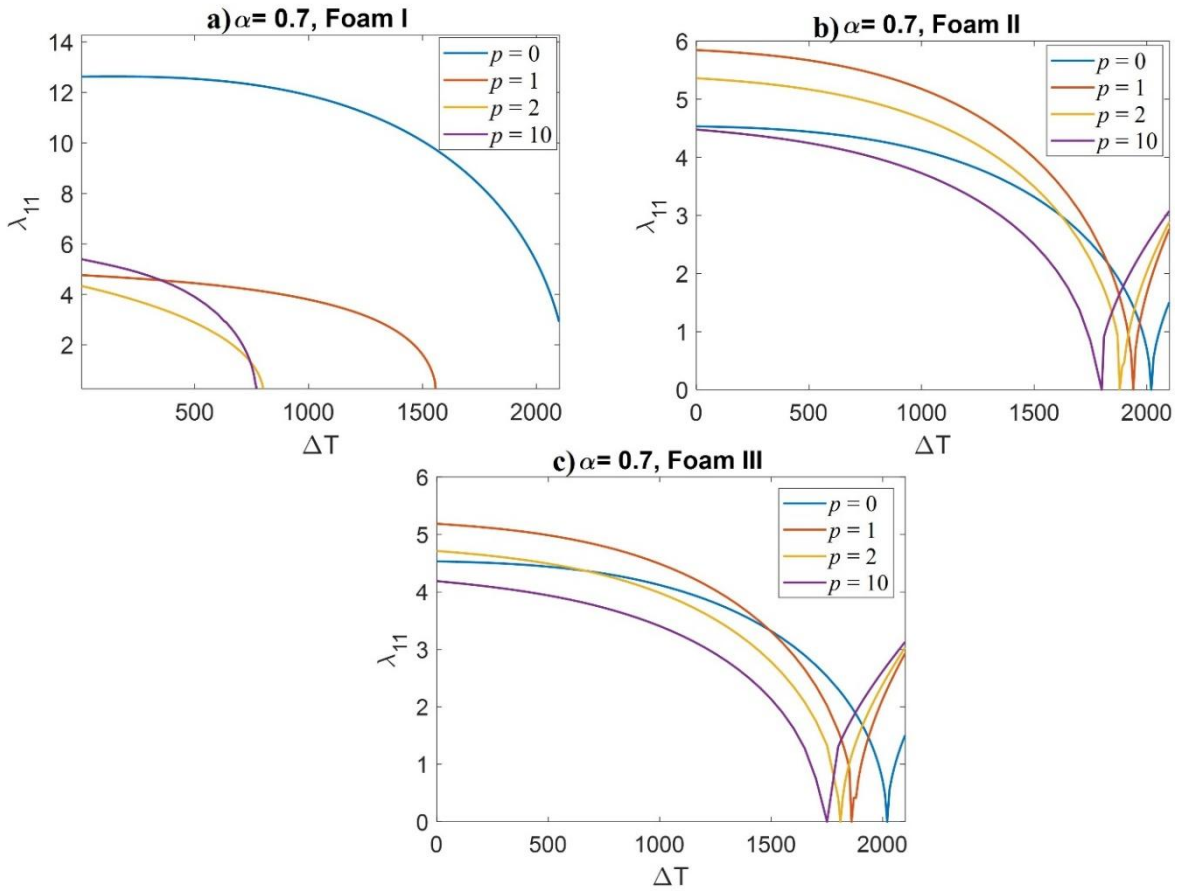

Figure 5. Comparison of the variation of the dimensionless fundamental frequency parameter $\lambda_{11}$with temperature rise $\Delta T$for different material gradation indices $p = 0,1,2,10$at porosity index $\alpha = 0.7$; aspect ratio $h = a/10$; electric potential parameter $V_m = 0$; magnetic potential parameter $H_m = 0$; nonlocal parameter $e_0 a = 0$; material length scale parameter $l_m = 0$. (a) FOAM I, (b) FOAM II, (c) FOAM III.

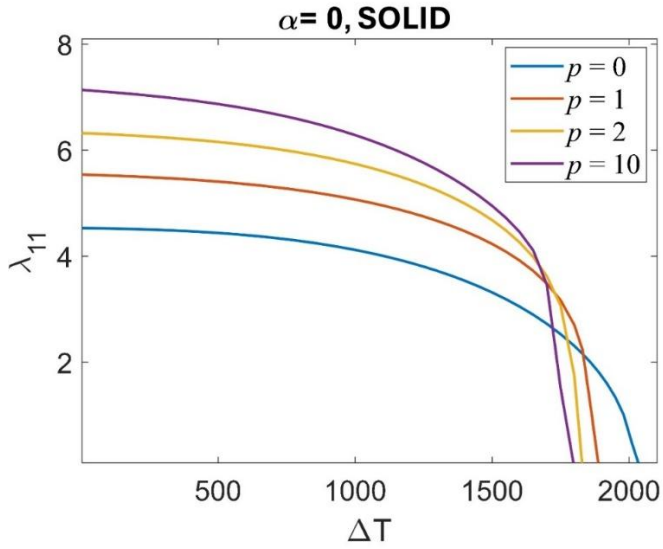

Figure 6. Variation of the dimensionless fundamental frequency parameter λ_{11} with temperature rise ΔT for different material gradation indices $p = 0, 1, 2, 10$ at porosity index $\alpha = 0$(solid core); aspect ratio $h = a/10$; electric potential parameter $V_m = 0$; magnetic potential parameter $H_m = 0$; nonlocal parameter $e_0 a = 0$; material length scale parameter $l_m = 0$.

4.3 Size-Dependent Behavior: Nonlocal and Strain-Gradient Effects

Figure 7 illustrates the influence of the nonlocal parameter $e_0a$on the dimensionless fundamental frequency parameter λ_{11} under increasing temperature rise for the solid configuration ($\alpha = 0$) with material gradation index $p = 1$. A clear stiffness softening effect is observed as the nonlocal parameter increases. For all temperature levels, higher values of $e_0a$systematically reduce the frequency parameter, confirming that long-range interatomic interactions weaken the effective structural rigidity in the nonlocal framework.

The influence of the nonlocal parameter becomes more pronounced at elevated temperature levels. As ΔTincreases, thermally induced in-plane compressive forces reduce the effective bending resistance of the nanoplate. When combined with nonlocal softening, this leads to an accelerated decay of $\lambda_{11}$and an earlier approach toward thermally induced instability. The curves indicate that larger nonlocal length scales shift the onset of rapid frequency reduction toward lower temperature values, demonstrating the strong coupling between scale effects and thermo-mechanical loading.

From the physical viewpoint, the nonlocal parameter is responsible for the stress attenuation phenomenon, where the stress at any point is affected not only by the strain at the same point but also by the surrounding stress field through the application of the nonlocal averaging procedure, leading to the attenuation of the stiffness of the material at the point of high strain gradients, particularly in the nano regime. As the thermal loading increases, the dynamic response is found to become highly sensitive to the geometric scale.

Although the above figure focuses attention on the nonlocal effect, the hybrid NSGT approach, as utilized in the current study, inherently includes the effects of the two length scale parameters, namely, the softening tendency of the material due to the nonlocal effect, as well as the hardening tendency of the material due to the strain gradient effect. It is evident from the results that the softening tendency of the material, as the value of e_0a increases, is predominant over the overall response, while the interaction between the two length scale parameters is found to affect the final stability limit of the nanoplate, thereby confirming the fact that the thermomechanical vibration response of the nanoplate is highly sensitive to the consideration of the long-range interactions as well as the strain gradient effect in the continuum approach.

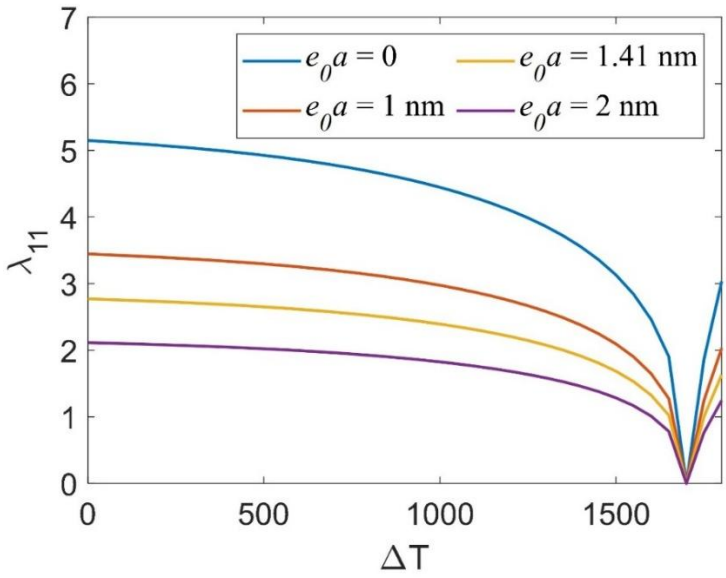

Figure 7. Variation of the dimensionless fundamental frequency parameter λ_{11} with temperature rise ΔT for different nonlocal parameters $e_0a = 0{,}1$ nm, 1.41 nm, 2 nm; aspect ratio $h = a/10$; porosity index $\alpha = 0$; material gradation index $p = 1$.

4.4 Influence of Magnetic Potentials

Figures 8 and 9 show the impact of the applied magnetic potential H_m on on the thermomechanical vibration response of the nanoplate. The results show that magnetic actuation can offer an effective method to increase stiffness in the nanoplate. As can be seen in Figure 8 for the fully $CoFe_2O_4$ case ($p = 0$), an increase in H_m results in an increase in the dimensionless fundamental frequency parameter λ_{11} over the entire range of temperature. In addition, the critical temperature at which rapid degradation in frequency occurs shifts to larger ΔT values as H_m is increased. This result reveals that magnetoelastic coupling can counteract thermally induced softening in the nanoplate.

In addition, a different result is observed in Figure 9, where λ_{11} is plotted versus H_m for different temperature rise cases. It can be observed that a linear increase in frequency is observed for all temperature rise cases. It should be noted that even as the temperature rise reduces the overall value of frequency, magnetic actuation enhances bending rigidity in the nanoplate.

From a physical perspective, the applied magnetic potential can induce magnetostrictive strains that can increase stiffness in the nanoplate. It should be noted that at elevated temperature, thermally induced in-plane compressive forces can reduce rigidity in the nanoplate. As a result, the magnetic potential can offer a counteractive effect to increase dynamic stability.

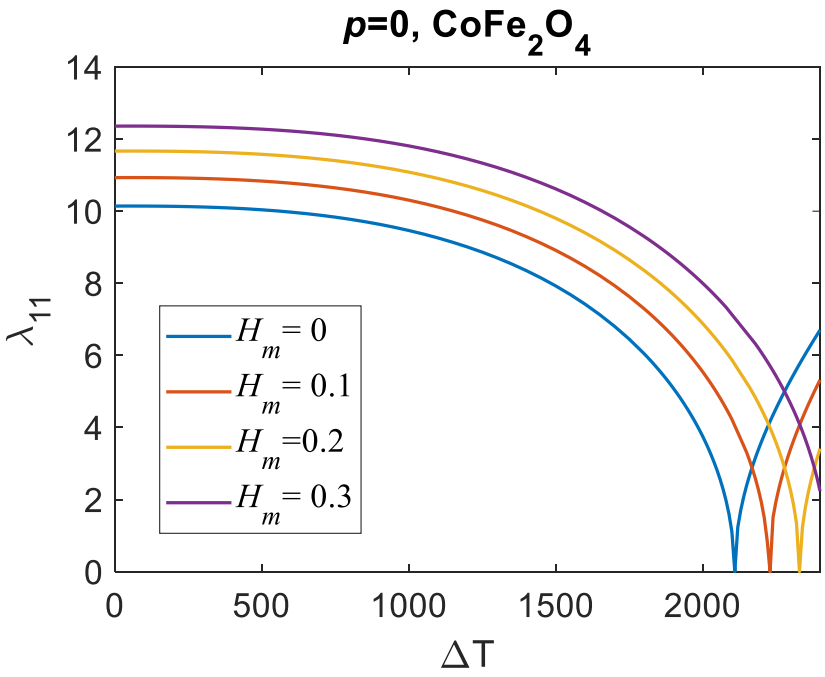

Figure 8. Variation of the dimensionless fundamental frequency parameter $\lambda_{11}$with temperature rise $\Delta T$for different magnetic potentials H_m = 0,0.1,0.2,0.3; ; aspect ratio $h = a/10$; porosity index $\alpha = 0$; material gradation index $p = 0$; electric potential parameter $V_m = 0$.

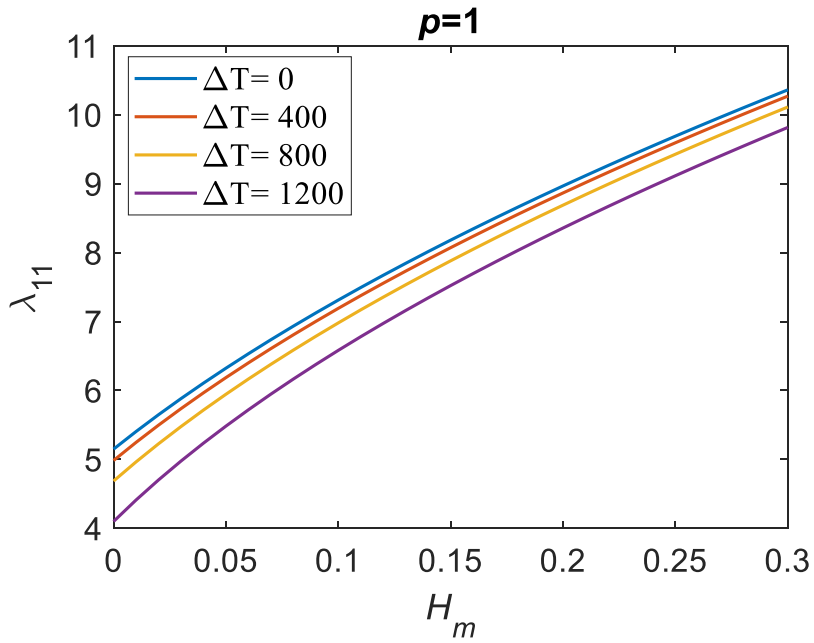

Figure 9. Variation of the dimensionless fundamental frequency parameter λ_{11} with magnetic potential H_m for different temperature rises ΔT = 0,400,800,1200; aspect ratio $h = a/10$; porosity index $\alpha = 0$; material gradation index $p = 1$; electric potential parameter $V_m = 0$.

4.5 Influence of Electric Potential

Figures 10 and 11 describe the role of the imposed electric potential V_m. Unlike magnetic actuation, the imposed electric potential introduces an effective softening term in the structural behavior.

Figure 10 shows that increasing the imposed electric potential reduces the fundamental frequency parameter for the graded structure ($p = 1$). Moreover, the onset of fast frequency decay due to thermal loading occurs at a lower temperature as the imposed electric potential increases. This behavior is more pronounced for increasing temperature loading, indicating a strong interaction between thermal loading-induced stresses and electroelastic effects.

Figure 11 presents the direct relationship between frequency behavior and the imposed electric potential. For all temperature loading cases, the parameter λ_{11} decreases linearly with increasing imposed electric potential. The rate of this reduction increases for increasing temperature loading. This behavior indicates that the softening mechanism induced by the imposed electric potential increases with temperature loading.

Physically, the imposed electric field induces electroelastic coupling stresses that act as a reduction in the effective bending stiffness of the current material configuration. When these additional stresses act in conjunction with temperature loading-induced compressive stresses, a more rapid reduction in stiffness occurs, leading to earlier instability.

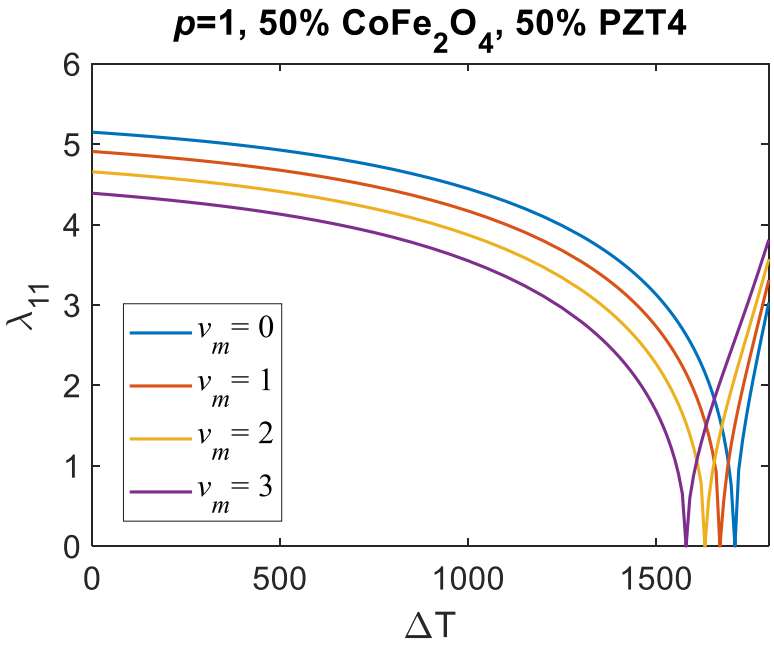

Figure 10. Variation of the dimensionless fundamental frequency parameter λ_{11} with temperature rise ΔT for different electric potentials $V_m = 0,1,2,3$; aspect ratio $h = a/10$; porosity index $\alpha = 0$; material gradation index $p = 1$; magnetic potential parameter $H_m = 0$.

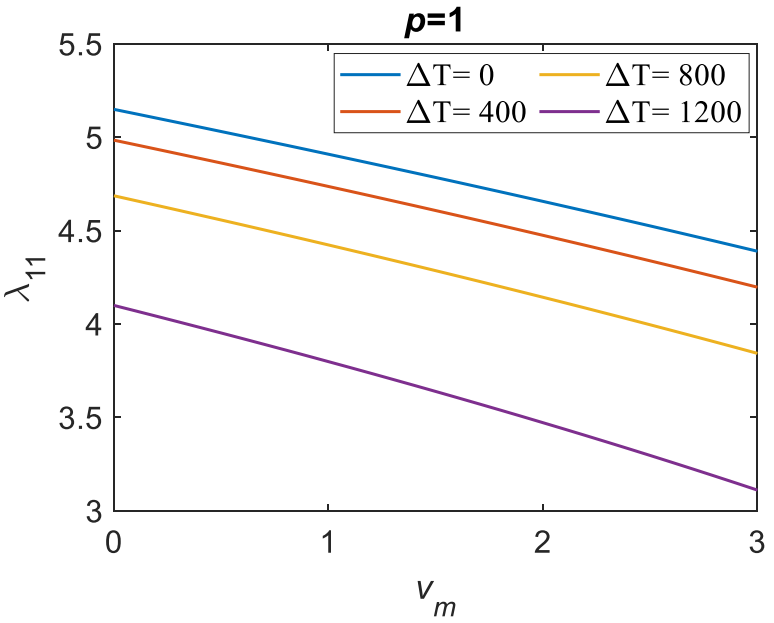

Figure 11. Variation of the dimensionless fundamental frequency parameter $\lambda_{11}$with electric potential $V_m$for different temperature rises $\Delta T = 0,400,800,1200$; aspect ratio $h = a/10$; porosity index $\alpha = 0$; material gradation index $p = 1$; magnetic potential parameter $H_m = 0$.

5. Conclusions

A comprehensive size-dependent thermomechanical vibration formulation for porous FG-MEE nanoplates has been developed in the context of nonlocal strain gradient theory. The model can

capture the effects of temperature-dependent properties, porosity distribution, functional gradation, as well as the interplay between electro-magnetic fields. This would facilitate a comprehensive assessment of the relative effects of softening and stiffening mechanisms at the nanoscale.

The results reveal that temperature elevation acts as a major destabilizing parameter, which reduces the effective stiffness due to material degradation as well as in-plane compressive stress caused by temperature elevation. The porosity parameter (α) has a significant influence in reducing the effective stiffness, thereby accelerating the onset of instability due to temperature elevation. The functional gradation parameter has a major influence in modulating the temperature sensitivity, as a lower gradation index leads to a higher level of stiffness as well as a slower rate of frequency degradation due to temperature elevation.

The size-dependent parameters play a crucial role in determining the dynamic behavior of the nanoplate. The nonlocal parameter leads to a reduction in effective stiffness, while the strain gradient parameter leads to a stiffening effect. These two effects must be considered simultaneously while determining the frequency evolution behavior for a nanoplate.

The results reveal that the magneto-electric coupling has a significant influence on dynamic behavior. The magnetic potential acts as a stiffening parameter, which increases the bending stiffness, delays the onset of instability due to temperature elevation, and acts as a stabilizing parameter. On the other hand, the electric potential acts as a softening parameter, which reduces the effective stiffness, decreases the frequency, as well as reduces the stability margin due to temperature elevation. The interplay between temperature elevation, electroelastic softening, as well as magnetoelastic stiffening determines the dynamic stability behavior of the nanoplate.

The formulation presented here can be considered a comprehensive model for predicting as well as controlling the thermomechanical vibration behavior of porous FG-MEE nanostructures. The results reveal the feasibility of controlling the frequency behavior through electro-magnetic fields. However, one must consider the Curie temperature for the piezoelectric as well as piezomagnetic materials for functional reliability at high temperature.

Data availabilitiy statement

Data will be made available on reasonable request.

Conflict of interest

The authors declare no conflicts of interest.

5. References

1. Monaco, G.T., Fantuzzi, N., Fabbrocino, F., and Luciano, R. (2021) Trigonometric solution for the bending analysis of magneto-electro-elastic strain gradient nonlocal nanoplates in hygro-thermal environment. *Mathematics*, **9** (5).

2. Aktas, K.G., Pehlivan, F., and Esen, I. (2024) Temperature-dependent thermal buckling and free vibration behavior of smart sandwich nanoplates with auxetic core and magneto-electro-elastic face layers. *Mech. Time. Depend. Mater.*, **28** (3), 1999–2039.

3. Chandel, V.S., Wang, G., and Talha, M. (2020) Advances in modelling and analysis of nano structures: A review. *Nanotechnol. Rev.*, **9** (1), 230–258.

4. Gholami, Y., Ansari, R., Gholami, R., and Sadeghi, F. (2022) Size-dependent free vibration and buckling analysis of magneto-electro-thermo-elastic nanoplates based on the third-order shear deformable nonlocal plate model. *Proc. Inst. Mech. Eng. C J. Mech. Eng. Sci.*, **236** (14), 8116–8133.

5. Esen, I., and Özmen, R. (2022) Thermal vibration and buckling of magneto-electro-elastic functionally graded porous nanoplates using nonlocal strain gradient elasticity. *Compos. Struct.*, **296**.

6. Barati, M.R., and Shahverdi, H. (2018) Frequency analysis of nanoporous mass sensors based on a vibrating heterogeneous nanoplate and nonlocal strain gradient theory. *Microsystem Technologies*, **24** (3), 1479–1494.

7. Saffari, P.R., Thongchom, C., Saffari, P.R., Lawongkerd, J., Keawsawasvong, S., and Senjuntichai, T. (2025) Free Vibration of Thermally Loaded FG-GPLRC Nanoplates Integrated with Magneto-Electro-Elastic Layers in Contact with Fluid. *International Journal of Structural Stability and Dynamics*, **25** (11), 2550113.

8. Fenjan, R.M., Hamad, L.B., and Faleh, N.M. (2020) Mechanical-hygro-thermal vibrations of functionally graded porous plates with nonlocal and strain gradient effects. *Adv. Aircr. Spacecr. Sci.*, **7** (2), 169–186.

9. Thai, C.H., Fereira, A.M.J., Nguyen-Xuan, H., Hung, P.T., and Phung-Van, P. (2023) A nonlocal strain gradient isogeometric model for free vibration analysis of magneto-electro-elastic functionally graded nanoplates. *Compos. Struct.*, **316**.

10. Yıldız, T., and Esen, I. (2024) The effect of the foam structure on the thermomechanical vibration response of smart sandwich nanoplates. *Mechanics of Advanced Materials and Structures*, **31** (28), 10279–10297.

11. Pehlivan, F., Esen, I., and Aktas, K.G. (2025) Thermomechanical Response of Smart Magneto-Electro-Elastic FGM Nanosensor Beams with Intended Porosity. *Arab. J. Sci. Eng.*, **50** (4), 2755–2777.

12. Esen, I., Abdelrhmaan, A., and Eltaher, M. (2021) Free vibration and buckling stability of FG nanobeams exposed to magnetic and thermal fields. *Eng. Comput.*, **38**, 3463–3482.

13. Momeni-Khabisi, H. (2022) Coupled thermal stability analysis of piezomagnetic nano-sensors and nano-actuators considering the flexomagnetic effect. *European Journal of Mechanics - A/Solids*.

14. Asrari, R., Ebrahimi, F., Kheirikhah, M., and Safari, K. (2020) Buckling analysis of heterogeneous magneto-electro-thermo-elastic cylindrical nanoshells based on nonlocal strain gradient elasticity theory. *Mechanics Based Design of Structures and Machines*, **50**, 817–840.

15. Tariq, A., Uzun, B., Deliktas, B., and Yaylı, M. (2024) Vibration analysis of embedded porous nanobeams under thermal effects using boosting machine learning algorithms and semi-analytical approach. *Mechanics of Advanced Materials and Structures*, **31**, 12320–12343.

16. Pham, Q.-H., Tran, V.K., and Nguyen, P.-C. (2023) Nonlocal strain gradient finite element procedure for hygro-thermal vibration analysis of bidirectional functionally graded porous nanobeams. *Waves in Random and Complex Media*, 1–32.

17. Lim, C.W., Zhang, G., and Reddy, J.N. (2015) A higher-order nonlocal elasticity and strain gradient theory and its applications in wave propagation. *J. Mech. Phys. Solids*, **78**, 298–313.

18. Thai, C., Ferreira, A., Nguyen-Xuan, H., and Phung-Van, P. (2021) A size dependent meshfree model for functionally graded plates based on the nonlocal strain gradient theory. *Compos. Struct.*, **272**, 114169.

19. Thai, C., Ferreira, A., and Phung-Van, P. (2020) A nonlocal strain gradient isogeometric model for free vibration and bending analyses of functionally graded plates. *Compos. Struct.*, **251**, 112634.

20. Farajpour, A., Yazdi, M., and Rastgoo, A. (2016) A higher-order nonlocal strain gradient plate model for buckling of orthotropic nanoplates in thermal environment. *Acta Mech.*, **227**, 1849–1867.

21. Abazid, M. (2019) The Nonlocal Strain Gradient Theory for Hygrothermo-Electromagnetic Effects on Buckling, Vibration and Wave Propagation in Piezoelectromagnetic Nanoplates. *Int. J. Appl. Mech.*

22. Thai, C.H., Hung, P.T., Nguyen-Xuan, H., and Phung-Van, P. (2023) A size-dependent meshfree approach for magneto-electro-elastic functionally graded nanoplates based on nonlocal strain gradient theory. *Eng. Struct.*, **292**.

23. Hùng, P., Phung-Van, P., and Thai, C. (2023) Small scale thermal analysis of piezoelectric–piezomagnetic FG microplates using modified strain gradient theory. *International Journal of Mechanics and Materials in Design*, 1–23.

24. Monaco, G.T., Fantuzzi, N., Fabbrocino, F., and Luciano, R. (2021) Critical Temperatures for Vibrations and Buckling of Magneto-Electro-Elastic Nonlocal Strain Gradient Plates. *Nanomaterials*, **11**.

25. Jandaghian, A., and Rahmani, O. (2016) Free vibration analysis of magneto-electro-thermo-elastic nanobeams resting on a Pasternak foundation. *Smart Mater. Struct.*, **25**.

26. Esen, I., and Özmen, R. (2024) Free and forced thermomechanical vibration and buckling responses of functionally graded magneto-electro-elastic porous nanoplates. *Mechanics Based Design of Structures and Machines*, **52** (3), 1505–1542.

27. Yang, F., Deng, Y., Wang, J., Huo, J., and Zhang, T. (2025) Post buckling behavior of porous magneto-electro-elastic nanoplates using nonlocal strain gradient theory. *Results in Engineering*.

28. Xu, L.-L., Chen, C.-P., and Zheng, Y.-F. (2025) Nonlinear chaotic dynamics analysis of magneto-electro-elastic laminated nanoplates considering flexomagnetoelectric effect in hygrothermal environments. *Journal of Vibration and Control*, **31**, 4472–4493.

29. Thai, C.H., Hung, P.T., Nguyen-Xuan, H., and Phung-Van, P. (2024) A free vibration analysis of carbon nanotube reinforced magneto-electro-elastic nanoplates using nonlocal strain gradient theory. *Finite Elements in Analysis and Design*, **236**.

30. Ozdemir, M.T., Das, T., and Esen, I. (2026) Effect of the hexachiral auxetic metamaterial on the 3D wave dispersion characteristics of sandwich nanoplate with foam FGM face layers. *ZAMM - Journal of Applied Mathematics and Mechanics / Zeitschrift für Angewandte Mathematik und Mechanik*, **106** (1).

31. Özmen, R. (2023) Thermomechanical vibration and buckling response of magneto-electro-elastic higher order laminated nanoplates. *Appl. Math. Model.*, **122**, 373–400.

32. Yıldırım, E., and Esen, I. (2025) Thermomechanical buckling of magneto-electro-elastic embedded smart sandwich nano plates. *International Journal of Mechanics and Materials in Design*, **21**, 701–736.

33. Ozdemir, M.T., Das, T., and Esen, I. (2025) Effect of the hexachiral auxetic structure on the thermal buckling behaviour of the magneto electro elastic sandwich smart nano plate using nonlocal strain gradient elasticity. *International Journal of Mechanics and Materials in Design*.

34. Salari, E., and Sadough Vanini, S.A. (2021) Investigation of thermal preloading and porosity effects on the nonlocal nonlinear instability of FG nanobeams with geometrical imperfection. *European Journal of Mechanics - A/Solids*, **86**, 104183.

35. Eroğlu, M., Esen, I., and Koç, M.A. (2023) Thermal vibration and buckling analysis of magneto-electro-elastic functionally graded porous higher-order nanobeams using nonlocal strain gradient theory. *Acta Mech.*, **235**, 1175–1211.

36. Ni, Y., Sun, J., Zhang, J., Tong, Z., Zhou, Z., and Xu, X. (2023) Accurate buckling analysis of magneto-electro-elastic cylindrical shells subject to hygro-thermal environments. *Appl. Math. Model.*

37. Liu, H., Baglioni, G., Boix-Constant, C., Van Der Zant, H., Steeneken, P., and Verbiest, G. (2023) Enhanced sensitivity and tunability of thermomechanical resonance near the buckling bifurcation. *2d Mater.*, **11**.

38. Šiškins, M., Keşkekler, A., Houmes, M., Mañas-Valero, S., Koperski, M., Coronado, E., Blanter, Y., Van Der Zant, H., Steeneken, P., and Alijani, F. (2023) Nonlinear dynamics and magneto-elasticity of nanodrums near the phase transition. *Nat. Commun.*, **16**.

39. Zhao, X., Zhu, W.-D., and Li, Y. (2020) Analytical solutions of nonlocal coupled thermoelastic forced vibrations of micro-/nano-beams by means of Green's functions. *J. Sound Vib.*, **481**, 115407.

40. Bellon, L., and Verlot, P. (2024) Temperature-mediated backaction in micromechanical and nanomechanical resonators. *Phys. Rev. B*.

41. Chiout, A., Brochard-Richard, C., Marty, L., Bendiab, N., Zhao, M.-Q., Johnson, A., Oehler, F., Ouerghi, A., and Chaste, J. (2023) Extreme mechanical tunability in suspended MoS_2 resonator controlled by Joule heating. *NPJ 2D Mater. Appl.*, **7**, 1–8.

42. Daikh, A.A., Drai, A., Bensaid, I., Houari, M.S.A., and Tounsi, A. (2021) On vibration of functionally graded sandwich nanoplates in the thermal environment. *Journal of Sandwich Structures & Materials*, **23** (6), 2217–2244.

43. Mahesh, V., Sagar, P., and Kattimani, S. (2017) Influence of coupled fields on free vibration and static behavior of functionally graded magneto-electro-thermo-elastic plate. *J. Intell. Mater. Syst. Struct.*, **29**, 1430–1455.

44. Ozalp, A.F., and Esen, I. (2025) Magnetic field effects on the thermomechanical vibration behavior of functionally graded biocompatible material sandwich nanobeams. *Mechanics of Advanced Materials and Structures*, **32** (3), 459–477.

45. Ozalp, A.F. (2025) Thermal buckling of doubly-curved FG sandwich shell with composite-foam core under Pasternak shear interaction. *Mech. Res. Commun.*, **150**, 104575.

46. Ozalp, A.F., and Esen, I. (2025) Vibration analysis of a hexachiral core and composite sandwich nanoplate resting on Pasternak foundation under magnetic thermal conditions. *Acta Mech.*, **236** (12), 7363–7384.

47. Kartaltepe, O., Kafali, A., and Esen, I. (2025) Thermo-mechanical vibration response of biocompatible sandwich nanoplates with a metamaterial hexachiral auxetic structure. *Mechanics Based Design of Structures and Machines*, 1–35.

48. Das, T., Ozdemir, M.T., and Esen, I. (2025) The effect of hexachiral auxetic metamaterial on the thermomechanical vibration response of doubly-curved sandwich nanoplates with foam FGM face layers. *ZAMM - Journal of Applied Mathematics and Mechanics / Zeitschrift für Angewandte Mathematik und Mechanik*, **105**.

49. Sobhy, M., and Radwan, A.F. (2023) Porosity and size effects on electro-hygrothermal bending of FG sandwich piezoelectric cylindrical shells with porous core via a four-variable shell theory. *Case Studies in Thermal Engineering*, **45**.

50. Wang, W., and Teng, Z. (2024) Analysis of vibration and critical buckling load of porous functionally graded material rectangular nanoplates under thermo-mechanical loading. *ZAMM Zeitschrift fur Angewandte Mathematik und Mechanik*, **104** (1).

51. Vinyas, M. (2020) On frequency response of porous functionally graded magneto-electro-elastic circular and annular plates with different electro-magnetic conditions using HSDT. *Compos. Struct.*, **240**.

52. Żur, K.K., Arefi, M., Kim, J., and Reddy, J.N. (2020) Free vibration and buckling analyses of magneto-electro-elastic FGM nanoplates based on nonlocal modified higher-order sinusoidal shear deformation theory. *Compos. B Eng.*, **182**.

53. Touloukian YS (1966) *(1966) Thermophysical properties of high temperature solid materials. Volume 4. Oxides and their solutions and mixtures. Part 1, vol 1.*, Macmillan, New York.

54. Ozalp, A.F., and Esen, I. (2025) Wave dispersion analysis with FGM face layers and GPL-reinforced metallic foam core thermally loaded sandwich nanoplate using NSGT. *Archive of Applied Mechanics*, **95** (9), 217.

55. Kafali, A., Kartaltepe, O., and Esen, İ. (2025) Vibration analysis of smart sandwich nanoplate incorporating butterfly auxetic core and piezoelectric face layers under thermal field. *Acta Mech.*

56. Tounsi, A., Houari, M.S.A., Benyoucef, S., and Adda Bedia, E.A. (2013) A refined trigonometric shear deformation theory for thermoelastic bending of functionally graded sandwich plates. *Aerosp. Sci. Technol.*, **24** (1), 209–220.

57. Bennoun, M., Houari, M.S.A., and Tounsi, A. (2016) A novel five-variable refined plate theory for vibration analysis of functionally graded sandwich plates. *Mechanics of Advanced Materials and Structures*, **23** (4), 423–431.

58. Ebrahimi, F., and Dabbagh, A. (2017) On flexural wave propagation responses of smart FG magneto-electro-elastic nanoplates via nonlocal strain gradient theory. *Compos. Struct.*, **162**, 281–293.

59. Das, T., Ozdemir, M.T., and Esen, I. (2025) The effect of the hexachiral auxetic metamaterial structure on the thermal buckling response of sandwich piezoelectric smart nanoplates. *Mechanics Based Design of Structures and Machines*, **0** (0), 1–37.

Appendix

$$\mathrm{K}_{11} = \left[1 + {l_m}^2\pi^2\left(\frac{m^2}{a^2} + \frac{n^2}{b^2}\right)\right]\left(-\frac{m^2\pi^2}{a^2}A_{11} - \frac{n^2\pi^2}{b^2}A_{66}\right)$$

$$\mathrm{K}_{12} = \left[1 + {l_m}^2\pi^2\left(\frac{m^2}{a^2} + \frac{n^2}{b^2}\right)\right]\left(-\frac{mn\pi^2}{ab}(A_{12} + A_{66})\right)$$

$$\mathrm{K}_{13} = \left[1 + {l_m}^2\pi^2\left(\frac{m^2}{a^2} + \frac{n^2}{b^2}\right)\right]\left(\frac{m^3\pi^3}{a^3}B_{11}^b + \frac{mn^2\pi^3}{ab^2}\left(B_{12}^b + 2B_{66}^b\right)\right)$$

$$K_{14} = \left[1 + {l_m}^2\pi^2\left(\frac{m^2}{a^2} + \frac{n^2}{b^2}\right)\right]\left(\frac{m^3\pi^3}{a^3}B_{11}^s + \frac{mn^2\pi^3}{ab^2}(B_{12}^s + 2B_{66}^s)\right)$$

$$K_{15} = \left[1 + {l_m}^2\pi^2\left(\frac{m^2}{a^2} + \frac{n^2}{b^2}\right)\right]\left(\frac{m\pi}{a}P_{11}\right)$$

$$K_{16} = \left[1 + {l_m}^2\pi^2\left(\frac{m^2}{a^2} + \frac{n^2}{b^2}\right)\right]\left(\frac{m\pi}{a}J_{11}\right)$$

$$K_{22} = \left[1 + {l_m}^2\pi^2\left(\frac{m^2}{a^2} + \frac{n^2}{b^2}\right)\right]\left(-\frac{m^2\pi^2}{a^2}A_{66} - \frac{n^2\pi^2}{b^2}A_{22}\right)$$

$$K_{23} = \left[1 + {l_m}^2\pi^2\left(\frac{m^2}{a^2} + \frac{n^2}{b^2}\right)\right]\left(\frac{m^2n\pi^3}{a^2b}\left(B_{12}^b + 2B_{66}^b\right) + \frac{n^3\pi^3}{b^3}B_{11}^b\right)$$

$$K_{24} = \left[1 + {l_m}^2\pi^2\left(\frac{m^2}{a^2} + \frac{n^2}{b^2}\right)\right]\left(\frac{m^2n\pi^3}{a^2b}(B_{12}^s + 2B_{66}^s) + \frac{n^3\pi^3}{b^3}B_{22}^s\right)$$

$$K_{25} = \left[1 + {l_m}^2\pi^2\left(\frac{m^2}{a^2} + \frac{n^2}{b^2}\right)\right]\left(\frac{n\pi}{b}P_{12}\right)$$

$$K_{26} = \left[1 + {l_m}^2\pi^2\left(\frac{m^2}{a^2} + \frac{n^2}{b^2}\right)\right]\left(\frac{n\pi}{b}J_{12}\right)$$

$$K_{33} = \left[1 + {l_m}^2\pi^2\left(\frac{m^2}{a^2} + \frac{n^2}{b^2}\right)\right]\left(-\frac{m^4\pi^4}{a^4}D_{11}^b - \frac{2m^2n^2\pi^4}{a^2b^2}\left(D_{12}^b + 2D_{66}^b\right) - \frac{n^4\pi^4}{b^4}D_{22}^b\right)$$
$$- \left[1 + \mu^2\pi^2\left(\frac{m^2}{a^2} + \frac{n^2}{b^2}\right)\right]\left[k_1 + k_2\pi^2\left(\frac{m^2}{a^2} + \frac{n^2}{b^2}\right)\right]$$
$$- \left(N_{px} + N_{Ex} + N_{Hx}\right)\frac{m^2\pi^2}{a^2} - \left(N_{py} + N_{Ey} + N_{Hy}\right)\frac{n^2\pi^2}{b^2}$$

$$K_{34} = \left[1 + {l_m}^2\pi^2\left(\frac{m^2}{a^2} + \frac{n^2}{b^2}\right)\right]\left(-\frac{m^4\pi^4}{a^4}D_{11}^s - \frac{2m^2n^2\pi^4}{a^2b^2}(D_{12}^s + 2D_{66}^s) - \frac{n^4\pi^4}{b^4}D_{22}^s\right)$$
$$- \left[1 + \mu^2\pi^2\left(\frac{m^2}{a^2} + \frac{n^2}{b^2}\right)\right]\left[k_1 + k_2\pi^2\left(\frac{m^2}{a^2} + \frac{n^2}{b^2}\right)\right]$$
$$- \left(N_{px} + N_{Ex} + N_{Hx}\right)\frac{m^2\pi^2}{a^2} - \left(N_{py} + N_{Ey} + N_{Hy}\right)\frac{n^2\pi^2}{b^2}$$

$$K_{35} = -\frac{m^2\pi^2}{a^2}P_{13} - \frac{n^2\pi^2}{b^2}P_{14}$$

$$\mathrm{K_{36}} = -\frac{\mathrm{m^2\pi^2}}{\mathrm{a^2}}\mathrm{J_{13}} - \frac{\mathrm{n^2\pi^2}}{\mathrm{b^2}}\mathrm{J_{14}}$$

$$K_{44} = \left[1 + {l_m}^2\pi^2\left(\frac{m^2}{a^2} + \frac{n^2}{b^2}\right)\right]\left(-\frac{m^4\pi^4}{a^4}H_{11}^s - \frac{2m^2n^2\pi^4}{a^2b^2}(H_{12}^s + 2H_{66}^s) - \frac{n^4\pi^4}{b^4}H_{22}^s\right.$$
$$\left. - \frac{m^2\pi^2}{a^2}A_{55}^s - \frac{n^2\pi^2}{b^2}A_{44}^s\right) - \left[1 + \mu^2\pi^2\left(\frac{m^2}{a^2} + \frac{n^2}{b^2}\right)\right]\left[k_1 + k_2\pi^2\left(\frac{m^2}{a^2} + \frac{n^2}{b^2}\right)\right]$$
$$- \left(N_{px} + N_{Ex} + N_{Hx}\right)\frac{m^2\pi^2}{a^2} - \left(N_{py} + N_{Ey} + N_{Hy}\right)\frac{n^2\pi^2}{b^2}$$

$$K_{45} = \left[1 + {l_m}^2\pi^2\left(\frac{m^2}{a^2} + \frac{n^2}{b^2}\right)\right]\left(-\frac{m^2\pi^2}{a^2}(P_{15} - P_{17}) - \frac{n^2\pi^2}{b^2}(P_{16} - P_{18})\right)$$

$$K_{46} = \left[1 + {l_m}^2\pi^2\left(\frac{m^2}{a^2} + \frac{n^2}{b^2}\right)\right]\left(-\frac{m^2\pi^2}{a^2}(J_{15} - J_{17}) - \frac{n^2\pi^2}{b^2}(J_{16} - J_{18})\right)$$

$$K_{55} = \left[1 + {l_m}^2\pi^2\left(\frac{m^2}{a^2} + \frac{n^2}{b^2}\right)\right]\left(\frac{m^2\pi^2}{a^2}P_{20} + \frac{n^2\pi^2}{b^2}P_{22} + P_{30}\right)$$

$$K_{56} = \left[1 + {l_m}^2\pi^2\left(\frac{m^2}{a^2} + \frac{n^2}{b^2}\right)\right]\left(\frac{m^2\pi^2}{a^2}J_{20} + \frac{n^2\pi^2}{b^2}J_{22} + J_{30}\right)$$

$$K_{66} = \left[1 + {l_m}^2\pi^2\left(\frac{m^2}{a^2} + \frac{n^2}{b^2}\right)\right]\left(\frac{m^2\pi^2}{a^2}S_{20} + \frac{n^2\pi^2}{b^2}S_{22} + S_{30}\right)$$